

AD-A046 951

ARGONNE NATIONAL LAB ILL ENGINEERING DIV
EXPERIMENTAL TWO-PHASE LIQUID-METAL MAGNETOHYDRODYNAMIC GENERAT--ETC(U)
SEP 77 M PETRICK, G FABRIS, E S PIERSON
ANL/MHD-77-3

F/G 10/2
N00014-76-F-0026
NL

UNCLASSIFIED

2
1 OF
ADA046951

The microfiche card contains a grid of 120 frames, arranged in 10 rows and 12 columns. The frames contain various technical data, including:

- Graphs: Several frames show plots of data, likely related to the experimental results. Some graphs show curves, while others show discrete data points.
- Tables: Multiple frames contain tables of numerical data, organized in columns and rows.
- Diagrams: Some frames include schematic diagrams or photographs of the experimental setup.
- Text: Frames contain blocks of text, likely providing context or descriptions for the data presented.

AD A 0 46951

RE. PAPER, PAPER, PAPER
P. 1
P. 2
P. 3
P. 4
P. 5
P. 6



RESEARCH REPORT
1972

OFFICE OF NAVAL RESEARCH

9 ANNUAL REPORT,
Aug 1975 - Sep 1976,

6 EXPERIMENTAL TWO-PHASE LIQUID-METAL
MAGNETOHYDRODYNAMIC GENERATOR PROGRAM

by

10

M. Petrick, Project Scientist

G. Fabris,
E. S. Pierson,
D. Carl
A. K. Fischer
C. E. Johnson

14 ANL/MHD-77-3

15 N00014-76-F-0026

ENGINEERING DIVISION

11 Sep 1977

12 95 p.

Approved for public release; distribution unlimited

410 027

mt

TABLE OF CONTENTS

	<u>Page</u>
LIST OF FIGURES.	v
LIST OF TABLES	vii
NOMENCLATURE	viii
DEFINITIONS.	x
SUMMARY	1
I. INTRODUCTION	2
II. TEST PROGRAM	5
II.1 Revised Ambient-Temperature NaK-Nitrogen Facility	5
II.2 NaK-Nitrogen Generator Experiments	9
II.3 Foams	9
III. GENERATOR PERFORMANCE	14
III.1 Repeat Runs at the Same Flow Rate	14
III.2 Comparison of New and Old Runs.	25
III.3 Reduced Back Pressure	29
III.4 Higher Flow Rates	36
IV. ANALYTICAL STUDIES OF ANNUALAR GENERATORS.	43
IV.1 Introduction	43
IV.2 Equations and Assumptions.	46
IV.3 Constant Velocity with no Armature Reaction.	49
IV.3.1 Analysis	49
IV.3.2 Numerical Examples	52
IV.4 Fully-Developed Laminar Flow with no Armature Reaction	55
IV.4.1 Analysis	55
IV.4.2 Numerical Examples	57

TABLE OF CONTENTS (Contd.)

	<u>Page</u>
IV.5 Armature Reaction with Constant Velocity	65
IV.5.1 Downstream Connection	65
IV.5.2 Upstream Connection	68
IV.5.3 Both Ends Connection	69
IV.5.5 Numerical Example	70
V. CONCLUSIONS AND FUTURE WORK	74
V.1 Higher Velocities and Pressures	75
V.2 Foams.	76
V.3 Improved Local Diagnostics	76
V.4 Analytical Models for the Two-Phase Flow in the Generator	77
V.5 Imperfect Compensation	77
REFERENCES	79
APPENDIX A Summary of Experimental Generator Data, August 1975 to September 1976	80

ACCESSION for	
NTIS	White Section <input checked="" type="checkbox"/>
DDC	Buff Section <input type="checkbox"/>
<small>UNCLASSIFIED U.S. SECURITY</small>	
<small>DISTRIBUTION/PY/ABILITY CODES</small>	
<small>SPECIAL</small>	
A	

LIST OF FIGURES

<u>No.</u>	<u>Title</u>	<u>Page</u>
I.1	Channel Contours Used in ANL LMMHD Experiments	3
II.1	NaK-Nitrogen Flow Loop	6
II.2	Bubble Behavior in Pure Mercury	12
II.3	Bubble Behavior in Mercury with 3 wppm Cesium	13
III.1	Liquid Velocity Along Generator, Open Circuit	15
III.2	Slip Ratio Along Generator, Open Circuit	16
III.3	Pressure Along Generator, Open Circuit	17
III.4	Load Factor Along Generator, Open Circuit	18
III.5	Void Fraction Along Generator, Open Circuit	19
III.6	Liquid Velocity Along Generator, $R_L = 0.27 \text{ m}\Omega$	20
III.7	Slip Ratio Along Generator, $R_L = 0.27 \text{ m}\Omega$	21
III.8	Pressure Along Generator, $R_L = 0.27 \text{ m}\Omega$	22
III.9	Local Load Factor Along Generator, $R_L = 0.27 \text{ m}\Omega$	23
III.10	Void Fraction Along Generator, $R_L = 0.27 \text{ m}\Omega$	24
III.11	Liquid Velocity Along Generator, 0.0058 Quality, Old and New Data	27
III.12	Liquid Velocity Along Generator, Reduced p_{st}	30
III.13	Slip Ratio Along Generator, Reduced p_{st}	31
III.14	Pressure Along Generator, Reduced p_{st}	32
III.15	Load Factor Along Generator, Reduced p_{st}	33
III.16	Void Fraction Along Generator, Reduced p_{st}	34
III.17	Generator Isentropic Efficiency vs. Quality at Different Pressures in the Separation Tank	35

LIST OF FIGURES (contd.)

<u>No.</u>	<u>Title</u>	<u>Page</u>
III.18	Liquid Velocity Along Generator, $\dot{m}_\ell = 11.91$ kg/s	37
III.19	Slip Ratio Along Generator, $\dot{m}_\ell = 11.91$ kg/s	38
III.20	Pressure Along Generator, $\dot{m}_\ell = 11.91$ kg/s	39
III.21	Local Load Factor Along Generator, $\dot{m}_\ell = 11.91$ kg/s	40
III.22	Void Fraction Along Generator, $\dot{m}_\ell = 11.91$ kg/s	41
III.23	Generator Isentropic Efficiency vs. Quality at Different Flow Rates	42
IV.1	Annular Generator Geometry	44
IV.2	Equivalent Circuit	50
IV.3	Velocity versus Radius as a Function of the Pressure Gradient, $R_o = 1.01$	58
IV.4	Velocity versus Radius as a Function of the Pressure Gradient, $R_o = 1.1$	59
IV.5	Velocity versus Radius as a Function of the Pressure Gradient for a Pump, $R_o = 0.01$	62
IV.6	Velocity versus Radius as a Function of the Pressure Gradient for a Pump, $R_o = 1.1$	63
IV.7	Load Connections for Armature Reaction Calculations	66
IV.8	Magnetic Flux Density at Inner Radius with Armature Reaction Versus Axial Location	72
IV.9	Current Density at Inner Radius with Armature Reaction Versus Axial Location	73

LIST OF TABLES

<u>No.</u>	<u>Title</u>	<u>Page</u>
III.1	Comparison of Generator Data with Old and Revised Loops, $\dot{m}_g = 6$ kg/s, Back Pressure = 0.14 MPa Gauge (20 psig)	26
IV.1	Open-Circuit Voltage and Excitation Ampere-Turns as a Function of Electrode Radii, Magnetic Field Strength at r_i , and Constant Velocity	53
IV.2	Powers per Meter Length for $r_i = 1$ m, $R_o = 1.1$, and Constant Velocity	54
IV.3	Powers per Meter Length and Efficiencies as a Function of the Pressure Gradient for $r_i = 3.0$ m, $R_o = 1.01$, $B_i = 3$ T, $V_L = 4$ V, and NaK	60
IV.4	Powers per Meter Length and Efficiencies as a Function of the Pressure Gradient for a Pump, $r_i = 0.5$ m, $R_o = 1.01$, $B_i = 2$ T, $V_L = 0.05$ V, and NaK	64
IV.5	Powers per Meter Length and Efficiencies as a Function of the Pressure Gradient for a Pump, $r_i = 0.5$ m, $R_o = 1.1$, $B_i = 2$ T, $V_L = 0.5$ V, and NaK	64
IV.6	Powers and Efficiencies With and Without Armature Reaction, $r_i = 1.0$ m, $R_o = 1.1$, $L = 1$ m, $u_z = 15$ m/s, $V_L = 3.903$, $F^i = 0.91$, $\sigma = 2.62 \times 10^5$ mhos/m, and $R_m = 4.939$	71

NOMENCLATURE

<u>SYMBOL</u>	<u>DEFINITION</u>
a	Electrode spacing
A	Area
B	Magnetic flux density
B_1	Magnetic flux density at $r = r_1$
C'_d	Bubble parameter
D_h	Hydraulic diameter
E	Electric field intensity
f	Friction factor
F	Load factor, $V_L/u_a aB$
F_{em}	Lorentz force on fluid
I_L	Load current
J	Current density
K	Slip ratio
L	Generator length
L'	Axial load current is zero at $z = L'$, both ends connection
\dot{m}_g	Mass flow rate of gas
\dot{m}_l	Mass flow rate of liquid
NI_{exc}	Ampere-turns to produce applied magnetic flux density
P	Pressure
P_{em}	Electromagnetic component of total pressure
P_{st}	Pressure in separator tank
P_v	Viscous component of total pressure

P_e	Electrical output power
P_m	Mechanical input power
P_r	Ohmic power loss
P_v	Viscous power loss
Q	Volumetric flow rate
r	Radius
r_i, r_o	Inner, outer electrode radii
R	Normalized radius ratio, r/r_i
R_i	Internal resistance of equivalent circuit
R_L	Load resistance
R_m	Magnetic Reynolds number, $\mu_o \sigma uL$
R_o	r_o/r_i
u	Velocity
u_g	Velocity of gas
u_l	Velocity of liquid
V_L	Load voltage
V_{oc}	Open-circuit voltage of equivalent circuit
α	Void fraction
η_g	Generator efficiency
η_p	Pump efficiency
μ	Absolute viscosity
μ_o	Permeability of free space
ρ	Density
σ	Electrical conductivity
x	Mixture quality, $\dot{m}_g/(\dot{m}_g + \dot{m}_l)$

Subscripts

r, θ, z Cylindrical coordinate system

DEFINITIONS

<u>NAME</u>	<u>SYMBOL</u>	<u>DEFINITION</u>
Bubble Parameter	C'_d	Empirical 'drag coefficient,' based on experimental data, used to calculate slip force between gas and liquid.
Load Factor	F	Ratio of load (electrode) voltage to induced voltage, $V_L/u_e aB$.
Void Fraction	α	Ratio of volume occupied by gas to total volume, or flow cross-sectional area occupied by gas to total cross-sectional area.
Mixture Quality	x	Ratio of gas mass flow rate to total mass flow rate, $\dot{m}_g/(\dot{m}_g + \dot{m}_l)$.
Slip Ratio	K	Ratio of gas to liquid velocity.

SUMMARY

The revised ambient-temperature NaK-nitrogen facility is described. The maximum liquid flow rate and generator inlet pressure are 10.9 kg/s (200 gpm) and 1.48 MPa absolute (200 psig), respectively, compared with the previous values of 6 kg/s (110 gpm) and 0.72 MPa absolute (90 psig). Satisfactory loop operation has been obtained, and new experiments with the second diverging-channel generator were completed. The principal experimental results were a higher power density for the same generator operating conditions, and an apparent tendency for the efficiency to improve more with increasing quality at higher velocities than at lower velocities.

An evaluation of an annular generator geometry is presented. The advantages and disadvantages of the geometry are described, the equations developed, and solutions obtained for three cases--constant velocity and no armature reaction, laminar flow with no armature reaction, and armature reaction with constant velocity. Numerical examples show that: (1) the attainable terminal voltages appear to be very low, (2) flow reversal and large viscous loss occur at or below the desired power densities, and (3) armature reaction effects are important and compensation techniques appear impractical. Thus, this annular geometry does not appear attractive for either generator or pump operation.

The initial steps in the program to produce and evaluate liquid-metal foams are described. The future directions of the experimental generator program, including foams, are discussed.

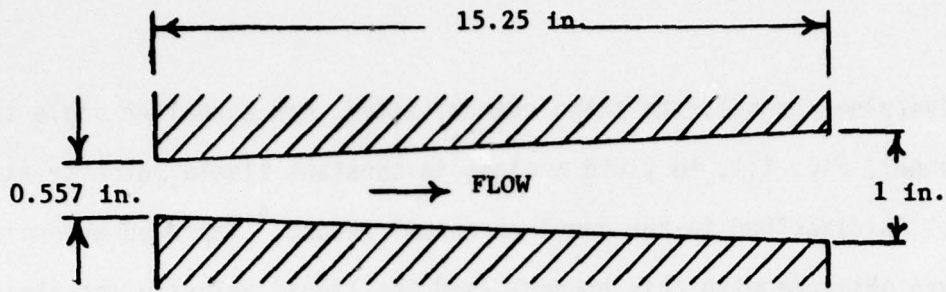
I. INTRODUCTION

The two-phase liquid-metal MHD generator program combines experimental and analytical studies in an effort to better understand the physical processes occurring in two-phase generators and to establish the limits of generator performance. For the past six years this program has been sponsored by the Power Branch of the Office of Naval Research.

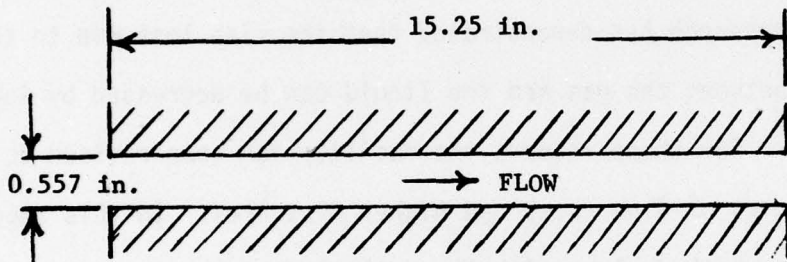
The generator experiments are conducted with an ambient-temperature NaK-N₂ test facility consisting of a two-phase mixer, MHD generator, magnet, and required auxiliary loop equipment. The original facility, used in all tests through July 1975, has been described elsewhere.¹ The revised facility, completed this year, is described in Section II.1 of this report. Earlier experiments on generators with varying geometries have been performed and the results presented in previous annual reports.^{2,3,4}

Analytical models of the generator have been developed to aid in the basic understanding of the flow characteristics in the generator and to provide a (one-dimensional) computer code which is capable of approximately predicting generator performance from the independent input parameters such as flow rate, magnetic field strength, and geometry. This computer code and the semi-empirical technique used to characterize the bubble parameter (churn-turbulent drag coefficient) used in the determination of the interfacial slip ratio have been reported in detail.^{2,5}

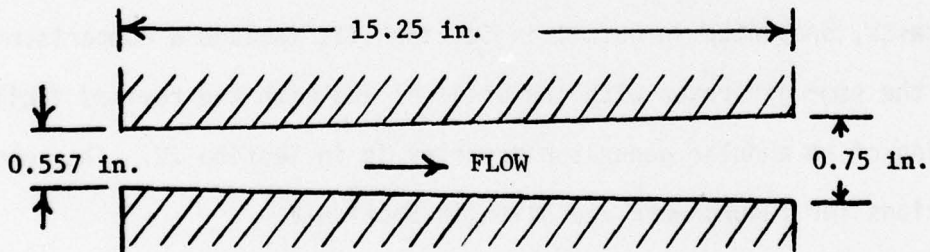
Previous generator experiments have used three different channels, Fig. I.1. The first channel was designed for a slip ratio of unity as the actual slip ratio was not known, but higher slip ratios were observed experimentally and the liquid velocity was not constant, decreasing along the generator.² Following this a constant-area channel was tested, and the velocity increased along the channel.^{2,3}



DIVERGING CHANNEL I



CONSTANT-AREA CHANNEL



DIVERGING CHANNEL II (present study)

Figure I.1. Channel Contours Used in ANL LMMHD Experiments

The second diverging channel, the third channel tested, has a smaller angle than the first channel, Fig. I.1, to yield a close-to-constant liquid velocity at the design point. As described in the previous annual report,⁴ improved generator performance was obtained with this channel, and the liquid velocity was almost constant.

Previous experiments have been limited to liquid velocities of about 12 m/s or less, smaller than anticipated for practical generators. In addition, recent experimental research has demonstrated that the slip loss due to the velocity difference between the gas and the liquid can be decreased by increasing the liquid velocity.³ For these reasons the facility has been revised to allow higher liquid velocities or flow rates and higher pressures. In this report the revised facility is described along with the initial data obtained with the second diverging channel in the revised facility, including some high-velocity runs.

The test program, described in Section II, consists of the facility revisions, the NaK-nitrogen tests, and the initial foam experiments. The results of the generator tests, presented in detail in Section III, include a comparison of runs using the same generator with the original and with the revised facilities. An evaluation of an annular generator geometry is in Section IV. The conclusions and suggestions for future work are given in Section V.

II. TEST PROGRAM

The experimental program is summarized in this section. The revised facility, designed for generator tests at higher liquid velocities and pressures, is described in Section II.1. The program for the NaK-nitrogen generator is in Section II.2, and the results are described in Section III. The initial experiments using surface-active agents to produce a foam are summarized in Section II.3.

II.1 Revised Ambient-Temperature NaK-Nitrogen Facility

The maximum liquid flow rate has been increased from 6 kg/s to 10.9 kg/s (110 gpm to 200 gpm), thus allowing generator tests at velocities anticipated to be typical of practical generators. As increasing the flow rate increases the pressure difference across the generator, the available generator inlet pressure was also increased from about 0.72 to 1.48 MPa absolute (90 to 200 psig).

The original loop was constructed primarily of two-inch pipe and had several two-inch globe valves that caused severe flow restrictions. In addition the pressure tanks did not have a high-enough pressure rating for some of the proposed tests. Thus, the loop was completely dismantled and rebuilt, as shown in Fig. II.1 for the NaK flow circuit. The major changes in the NaK circuit were:

1. Two new canned-rotor NaK pumps were added in series with the existing pump. The three pumps produce a gross pressure difference of 1.57 MPa (228 psi) at 10.9 kg/s (200 gpm). For experiments where the total pump capacity is not required, one or two pumps may be bypassed.

2. The existing separation and supply tanks were replaced by a single, larger tank with a rated pressure of 1.31 MPa absolute (175 psig). It has internal baffles enabling it to separate twice the NaK and nitrogen flow rate

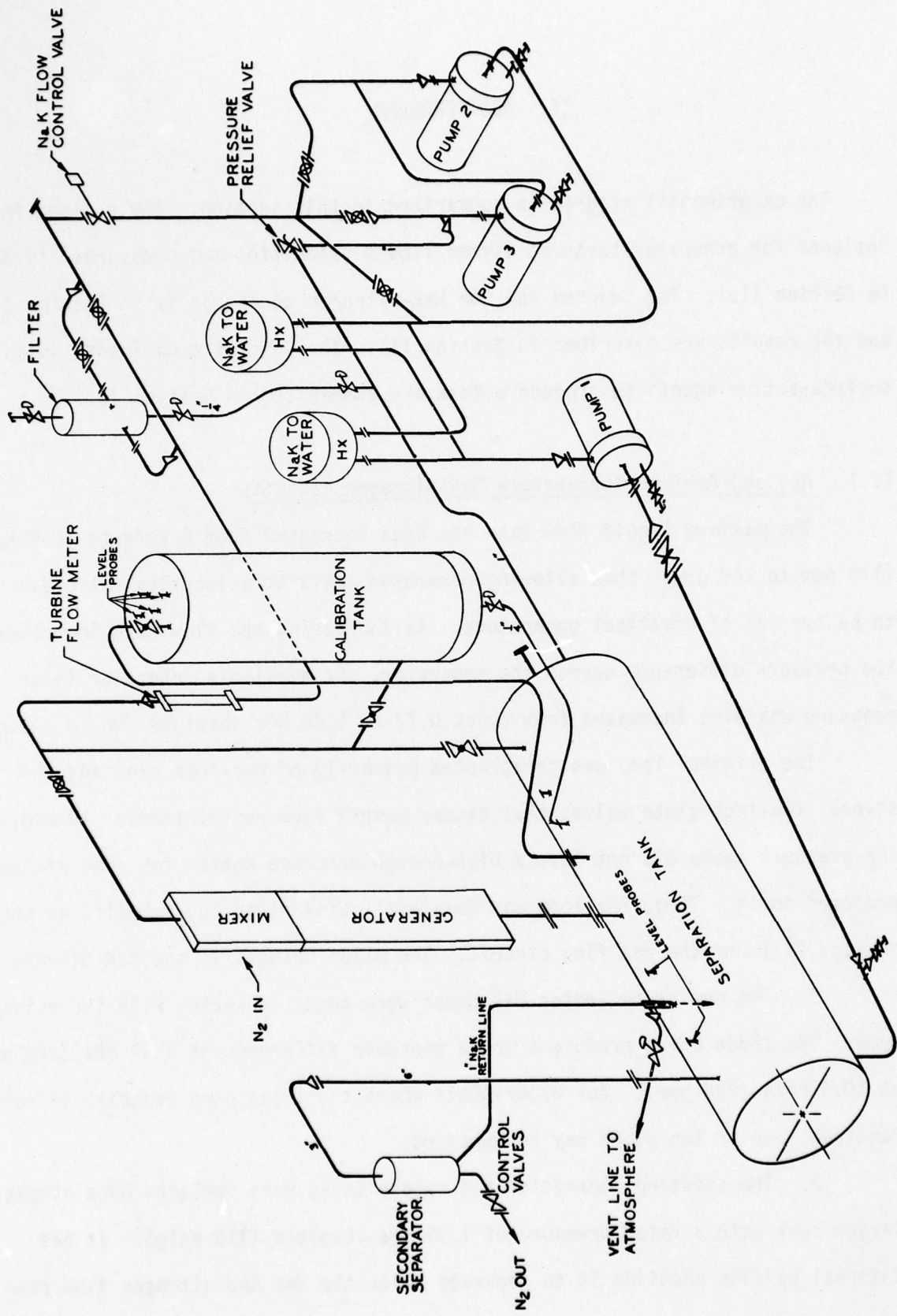


Figure II.1. NaK-Nitrogen Flow Loop

of the old tanks. A vortex suppressor consisting of a three-inch inner pipe surrounded by a five-inch outer pipe so that the NaK flows up the annulus between the two pipes and down the inner pipe into the line to the pumps was installed in the tank.

3. The calibration tank was replaced by a larger one of 210 kg NaK capacity and a rated pressure of 2.14 MPa absolute (295 psig).

4. The 150 psi NaK filter housing was replaced by a 300 psi housing.

5. The air-cooled heat exchanger was replaced with two water-cooled heat exchangers connected in parallel. This eliminated the pressure loss of the previous heat exchanger, and provides sufficient cooling capacity for year-round operation. (In fact, in warm weather the loop can now be made cool enough to condense moisture on the NaK pipes. Before, operation had to be curtailed in warm weather.)

6. Most of the two-inch piping was eliminated, and the NaK flow control is now provided by a three-inch air-operated valve rather than a two-inch manual globe valve. All non-control valves are ball valves, except for a four-inch Y-pattern globe valve in the inlet line to the first pump.

7. Most new components are carbon steel as stainless steel is not required for a room-temperature NaK facility.

8. All kerosene cooling was eliminated, and the magnet and load resistor are cooled by water. This prevents the possibility of a combined NaK and kerosene fire.

9. Some minor NaK carryover with the nitrogen from the separator tank was observed. A three-inch commercial secondary separator has been ordered and will be installed in the six-inch exhaust line.

Changes completed in the nitrogen circuit include:

1. The nitrogen purifier (NaK bubbler) tank was hydrostatically tested to increase its pressure rating.

2. An electrically-operated valve to shut off the nitrogen supply in case of an emergency and a new pressure relief valve were installed.

3. Some pipe sections and valves were replaced to reduce the number of bends and fittings, and the pipe length, and thus reduce the pressure drop.

4. A proportional controller for the nitrogen exhaust valves was added to hold the pressure constant in the separator tank.

Extra nitrogen heater capacity will be required in the future for the higher flow rates.

The modified loop allows two modes of operation that were not possible before. These are:

1. Operation at up to 10.9 kg/s (200 gpm) NaK flow with a corresponding increase in the nitrogen flow to determine the effect of liquid velocity on slip and generator efficiency. Extra capacity is available and operation at up to 18 kg/s NaK flow is possible.

2. Variable back pressure at the generator exit, up to 1.14 MPa absolute (150 psig) at reduced flow rates, to determine the effect of back pressure on generator performance. In this mode only one or two pumps may be used to avoid excessive pressure. Operation at low back pressures, down to about 0.12 MPa absolute (17 psia), is also possible, and this allows larger pressure ratios across the generator. (The old facility was limited to pressures above about 0.24 MPa absolute due to the high pressure drop between the separator tank and the suction side of the pump.)

Several safety features are incorporated into the modifications. The piping is designed for 2.0 MPa absolute (275 psig) and the separation/storage tank for 1.31 MPa absolute (175 psig). Pressure switches stop or prevent from starting one, two, or all three pumps if pre-set pressures in the separation tank or high-pressure piping are exceeded. The separation and nitrogen purifier tanks are protected by safety valves, as before, but with higher pressure ratings. Emergency switches to turn off the NaK pumps and the nitrogen supply were placed on the main control panel and adjacent to two doors. A future remove valve for the cooling-water supply has been provided for in the control panel.

II.2 NaK-Nitrogen Generator Experiments

The significant parameters for all of the experimental runs for the period from August 1975 through September 1976 are summarized in Appendix A. The runs were chosen to give operating experience with the revised facility, determine the limits of the facility, and allow comparison of measurements with the original and revised facilities to see if there were any changes. The data, as discussed in Section III, showed a significant improvement in generator performance with the revised facility.

II.3 Foams

The slip loss due to the relative phase velocities is presently one of the major loss mechanisms in two-phase liquid-metal MHD generators, especially at the high void fractions required for efficient cycle operation. One method of reducing this loss is to produce a more-stable foam flow by means of surface-active agents. The potential gains in generator and cycle performances make this approach very attractive. Thus, a program to evaluate surface-active agents has been initiated. The major points are:

1. Locate suitable agents for the liquid metals of practical interest.
2. Determine the techniques required for adequate separation of the phases after the generator.
3. Perform tests in an MHD generator.

There is a lack of data in the literature characterizing the preparation and properties of a liquid-metal foam of the desired kind, although the available literature on the characterization of aqueous and organic forms has given some insight into the preparation of a liquid-metal foam. In this literature there was frequent reference to the use of surfactant additives, and surface tension and viscosity appeared to be the relevant physical properties of interest. Therefore, scoping studies focused on the effect of surfactants as liquid-metal foam inducers and the potential for fine particle suspensions to act as foam promoters have been initiated. Viscosity was selected as the measured physical property for use in correlation of systems of differing bubble behavior. In later studies measurements of surface tension will be included.

An experimental facility for studying surfactants in room-temperature NaK has been built. Initially, the emphasis will be on visual observations in Pyrex vessels of the foaming behavior when nitrogen is bubbled through. A glovebox was opened, cleaned thoroughly, and a new balance and the gas system for handling ultra-high-purity nitrogen were installed. Safety of the NaK operations was reviewed. An apparatus for transferring NaK was designed and built.

While waiting for the high-purity NaK, experiments were done with mercury to obtain experience with the facility and to develop a "feel" for foam behavior in liquid metals, and encouraging results were obtained. The mercury was held in a Pyrex vessel. An upturned tube made of copper or of polyethylene having

a 0.054 cm orifice was used as the gas bubbler. Visual observations were made of the system behavior and a flow rate of 5 cc/min was adopted as a standard condition. Differences in bubble size were noted when the bubbles were formed from the polyethylene tube as compared with those formed by the copper bubbler. The size differences most certainly relate, at least in part, to differences in the wetting characteristics of the two materials. This observation suggests that the wetting behavior between the liquid metal and the mixer may be an important design consideration in a LMMHD generator.

A system that was found to show some enhancement of bubble lifetime was one having one wt % cadmium in mercury. Motion pictures were made of the bubble action (45 frames/second). The most outstanding enhancement of bubble lifetime occurred when cesium at a concentration of 3 wppm was used as the surfactant. For this mixture (Cs in Hg) up to seven coexisting bubbles were seen, with a group of six showing lifetimes up to 10 seconds after the gas flow was stopped. Figures II.2 and II.3, excerpted from the movie, illustrate the difference in bubble behavior in the absence and in the presence of cesium. Higher concentrations of cesium were also effective, but not to the same degree. These observations demonstrate the potential for developing a liquid metal foam system suitable for LMMHD application.

The initial experiments with NaK will focus on the ability of fine particle dispersions to promote bubble lifetime. Earlier work had indicated that carbon black dispersed in NaK had apparently altered the surface properties.



Figure II.2. Bubble Behavior in Pure Mercury

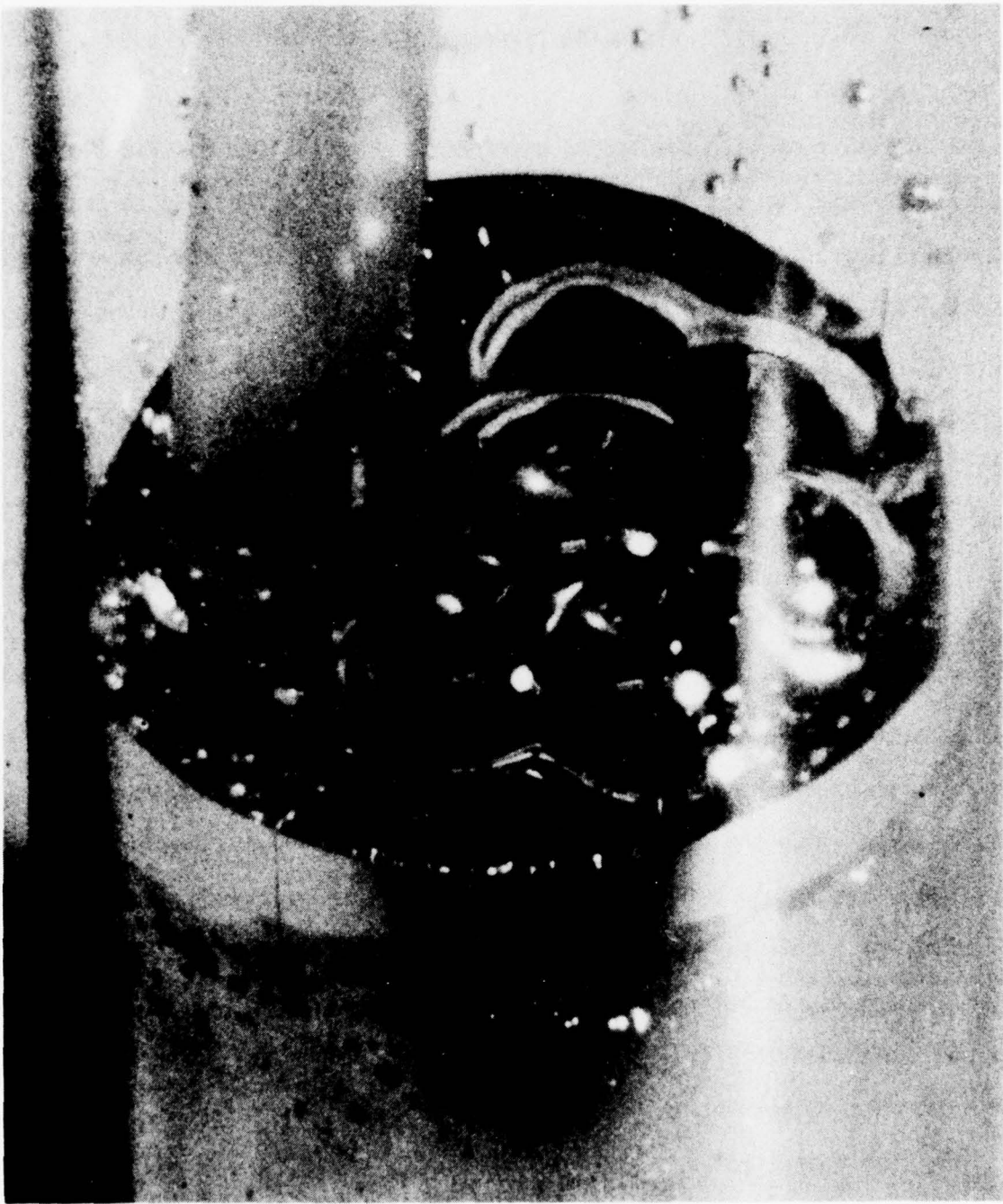


Figure II.3. Bubble Behavior in Mercury with 3 wppm cesium

III. GENERATOR PERFORMANCE

The initial runs with the second divergent channel in the revised flow facility were made for the same conditions as with the old facility to provide a check on the operation of the facility. Some of these results are summarized in Section III.1. A detailed comparison for one set of new and old runs for the same operating parameters is given in Section III.2. The effects of reduced back pressure and higher flow rates are discussed in Sections III.3 and III.4, respectively. A summary of all of the experimental data for the period from August 1975 to September 1976 is given in Appendix A.

III.1 Repeat Runs at the Same Flow Rate

The liquid velocity, slip ratio, pressure, local load factor, and void fraction versus distance along the generator are plotted in Figs. III.1 through III.5 for one set of open-circuit runs. No major change with respect to the appropriate runs with the old facility, in 1975, was observed. The void fractions are somewhat higher than before, and this is probably connected with the reduced slip and higher bubble parameter (drag coefficient), as discussed in the next section. There is, as before, an unusually-high pressure gradient at the generator midsection, although this time it seemed less pronounced, and a pronounced drop in the load factor, both at the higher void fractions.

The same quantities are plotted in Figs. III.6 to III.10 for a generator with a load resistance of $R_L = 0.27 \text{ m}\Omega$. Again, the variations are similar to the results obtained in July 1975. However, the pressure gradient for the high-void-fraction runs appeared to be more uniform than previously. There is still a pronounced decrease in the local load factor with increasing void

$m_e = 6 \text{ kg/s}$
 $B_e = 1.245 \text{ T}$
 $R_L = \infty$
 $p_{st} = 20 \text{ psia}$

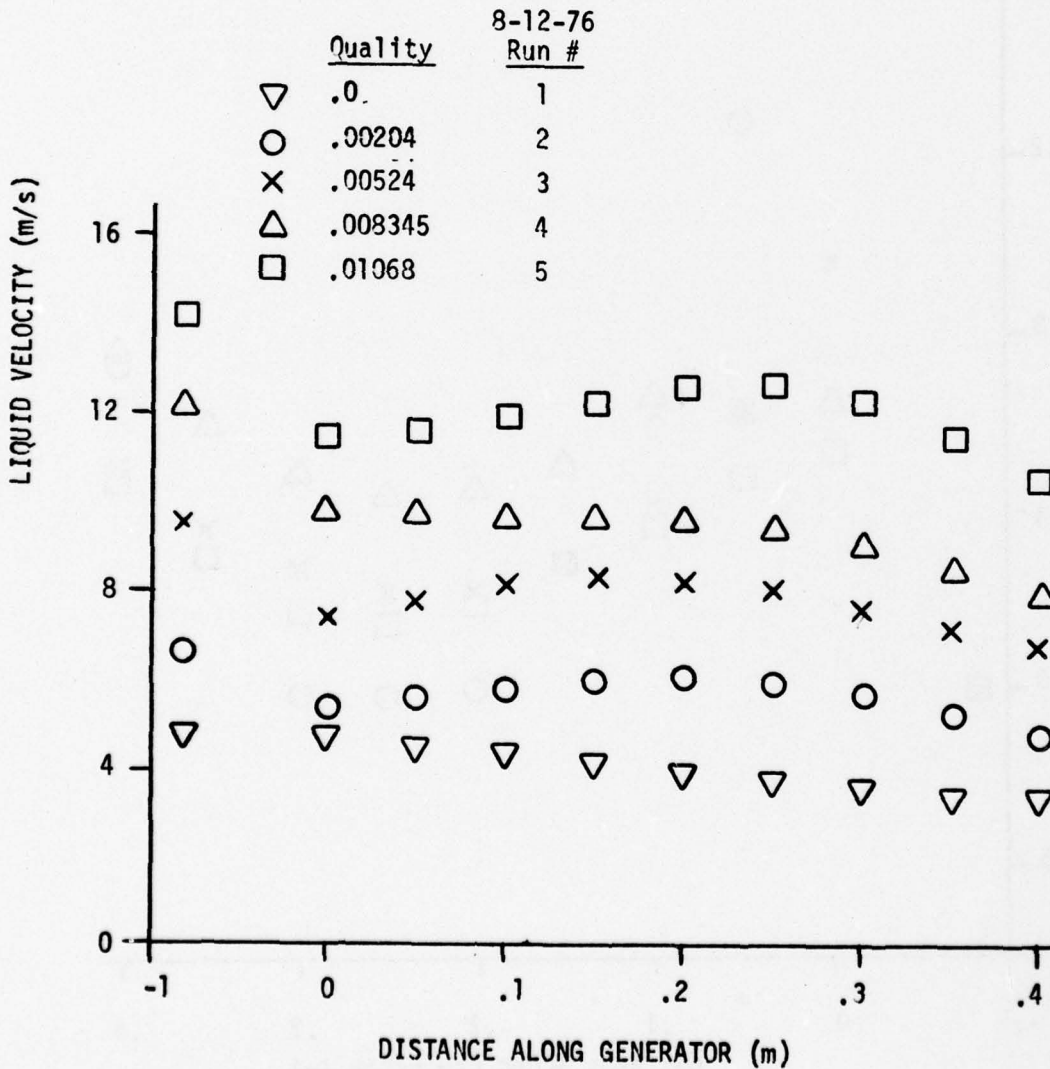


Fig. III.1 Liquid Velocity Along Generator, Open Circuit

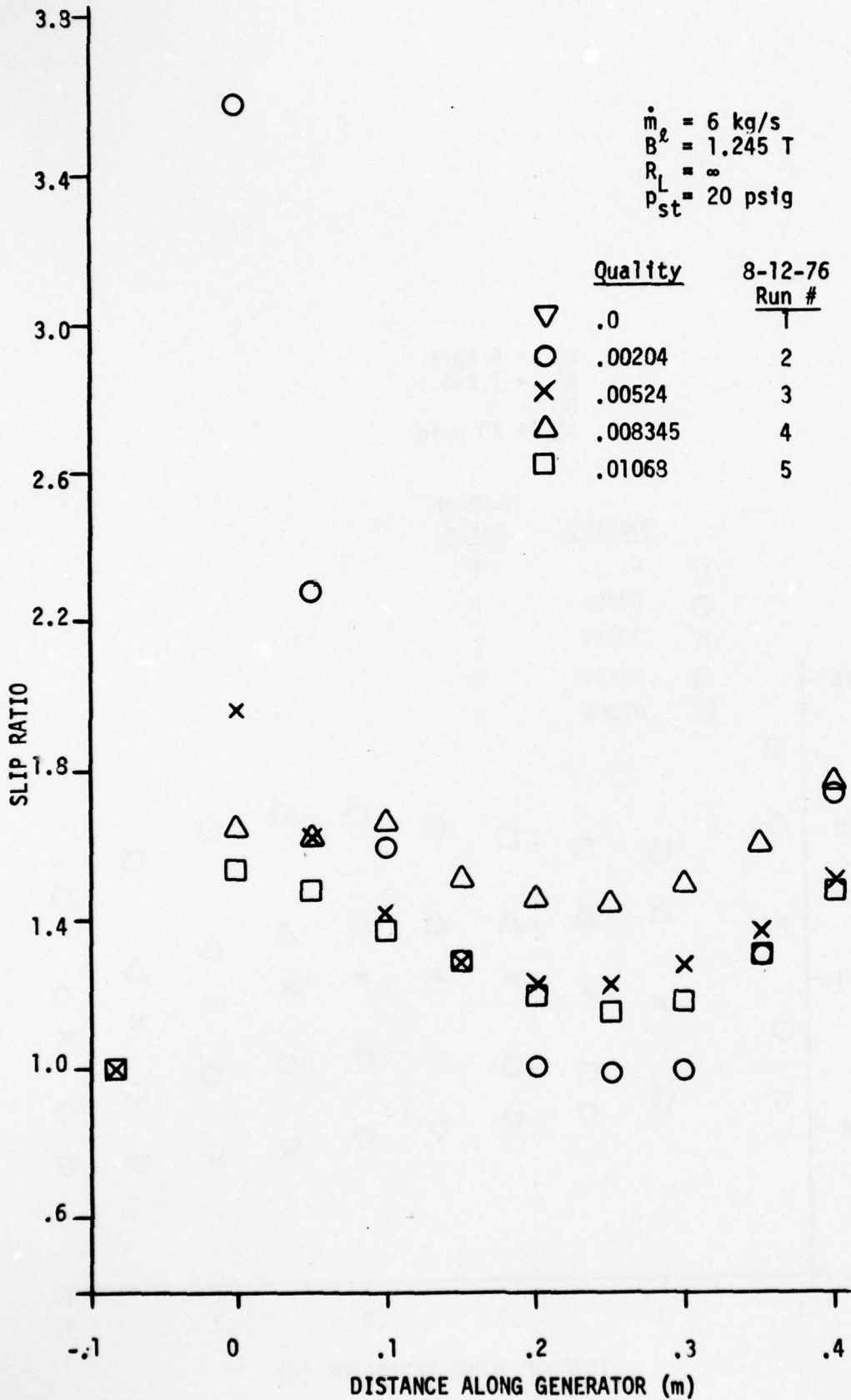


Figure III.2 Slip Ratio Along Generator, Open Circuit

\dot{m} = 6 kg/s
 B^2 = 1.245 T
 R_L = ∞
 p_{st} = 20 nsig

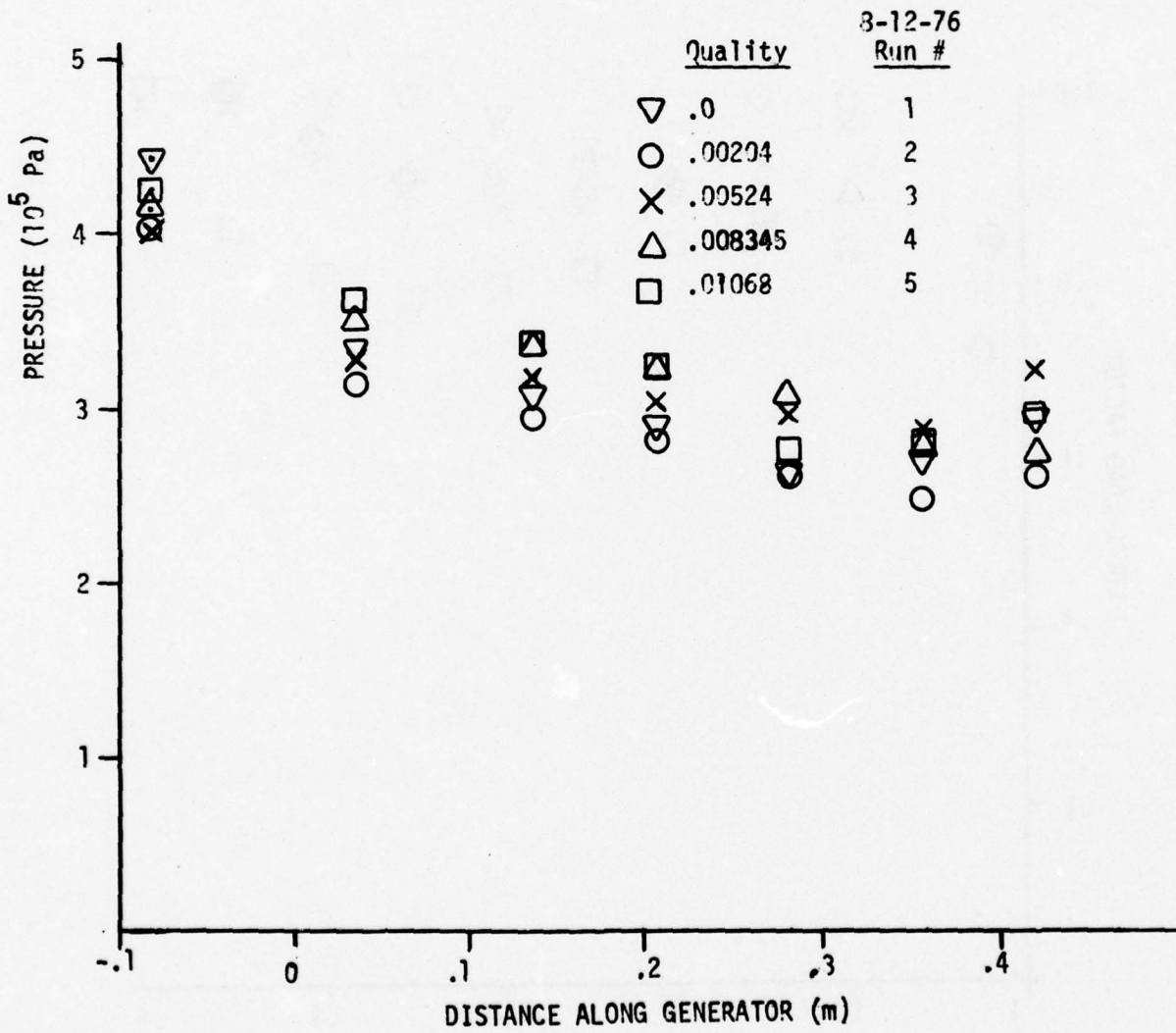


Figure III.3 Pressure Along Generator, Open Circuit

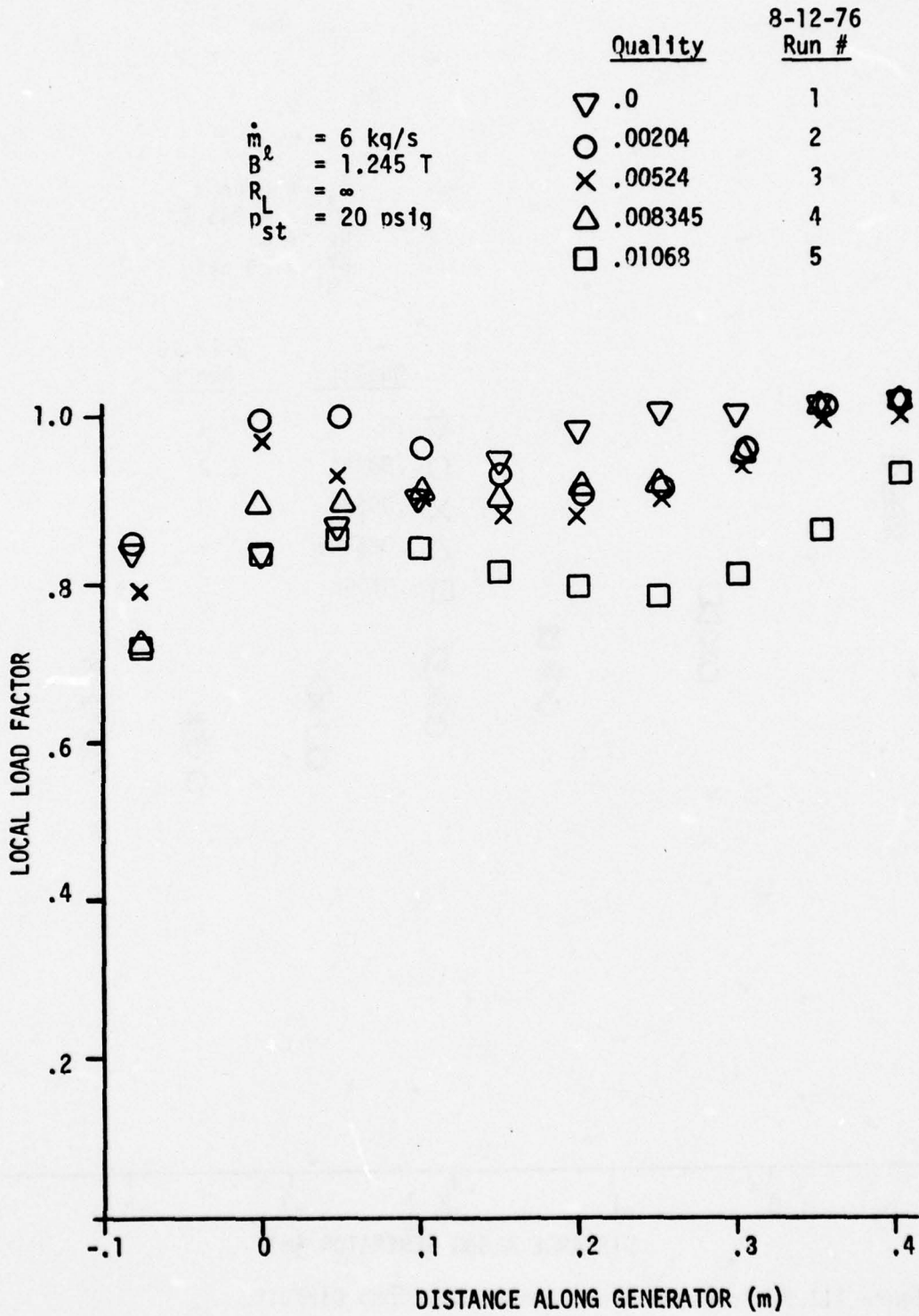


Figure III.4 Load Factor Along Generator, Open Circuit

$\dot{m}_l = 6 \text{ kg/s}$
 $B^l = 1.245 \text{ T}$
 $R_L = \infty$
 $p_{st} = 20 \text{ psig}$

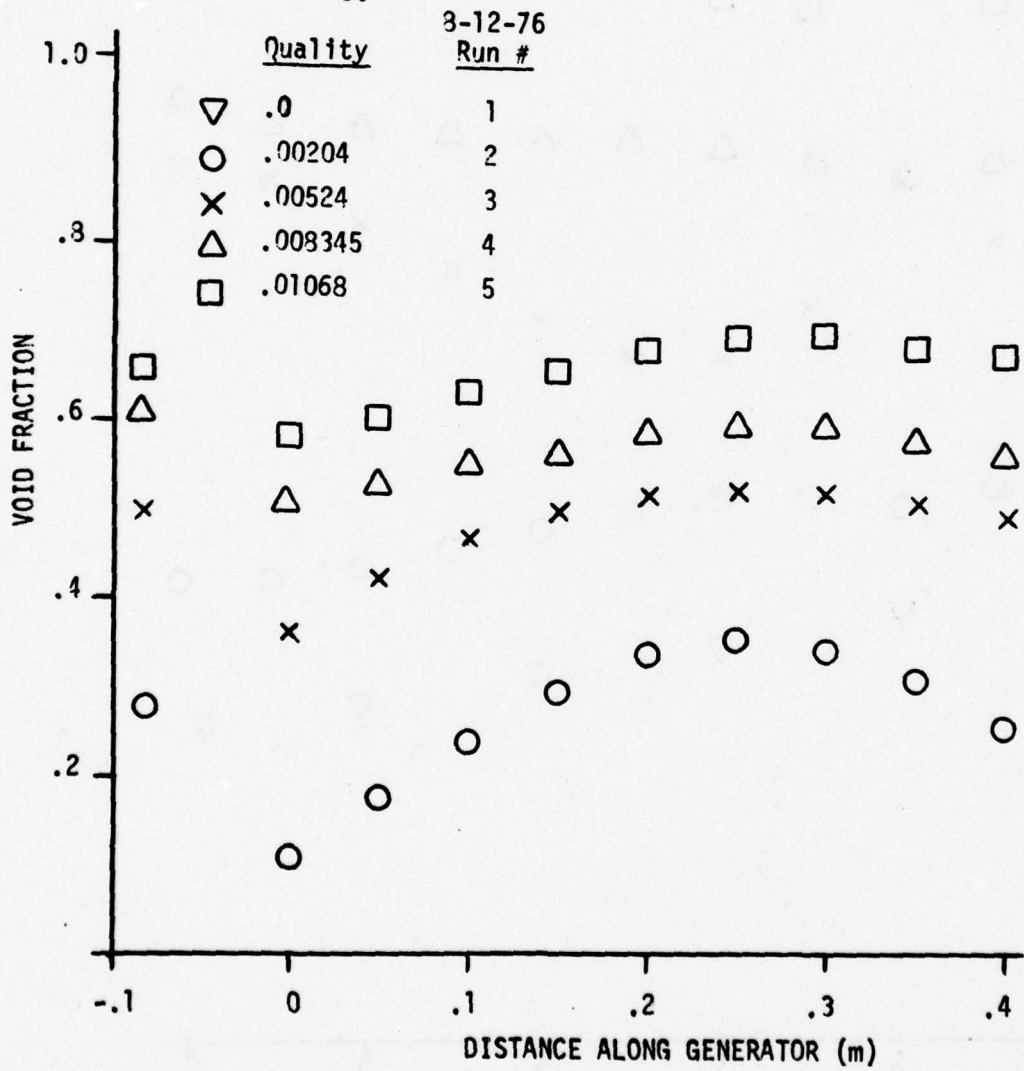


Figure III.5 Void Fraction Along Generator, Open Circuit

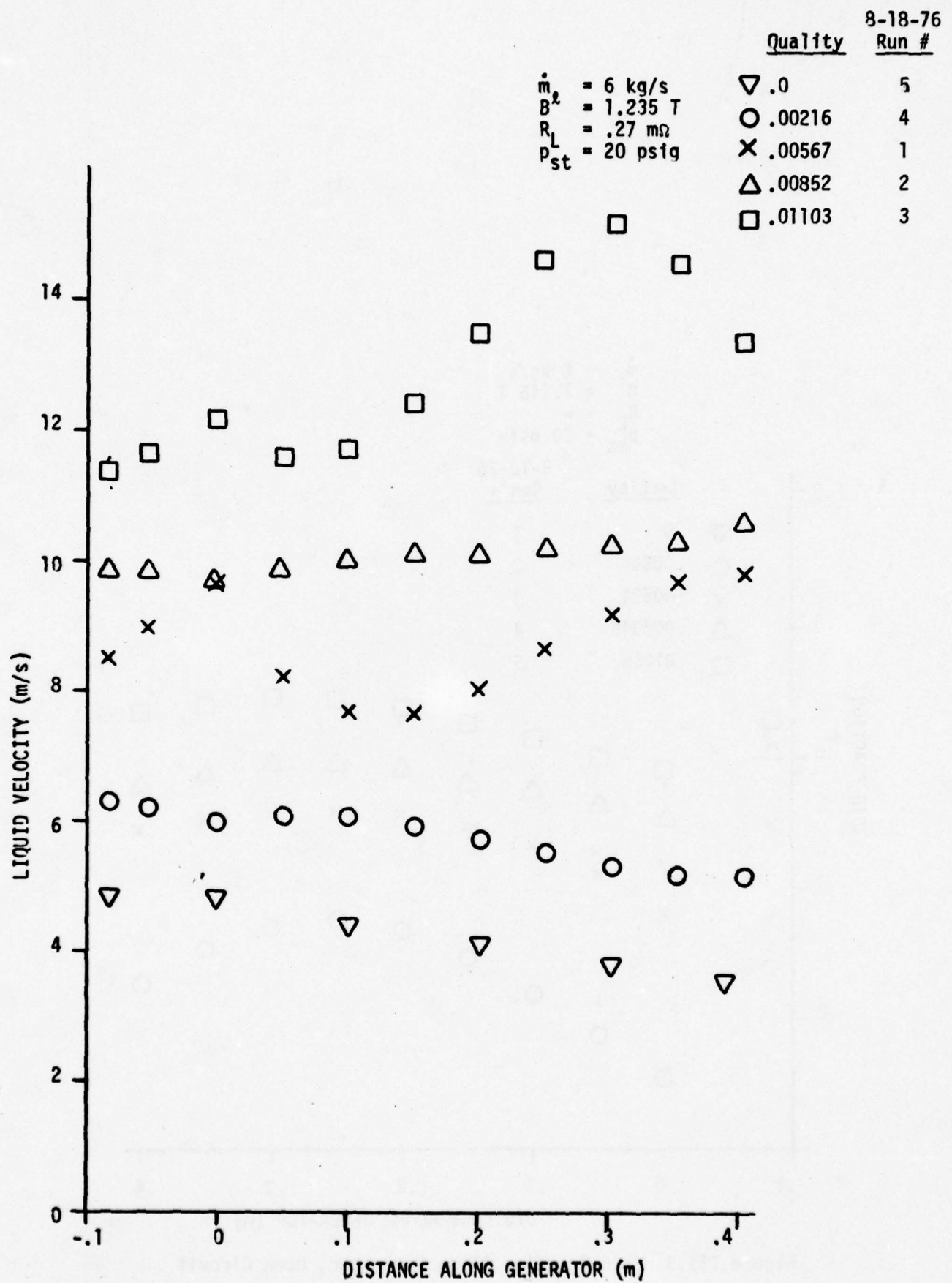


Figure III.6 Liquid Velocity Along Generator, $R_L = 0.27 \text{ m}\Omega$

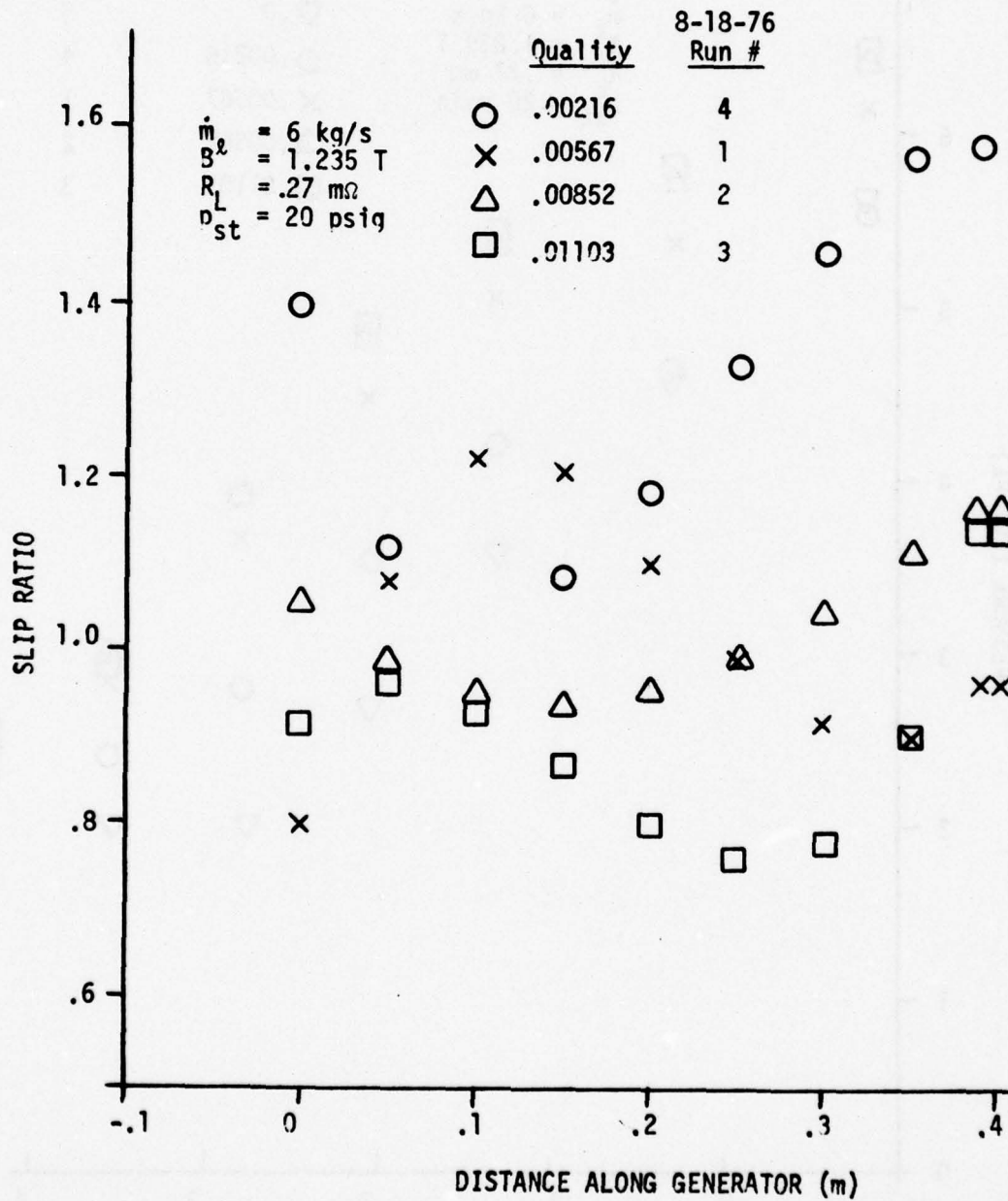


Figure III.7 Slip Ratio Along Generator, $R_L = 0.27 \text{ m}\Omega$

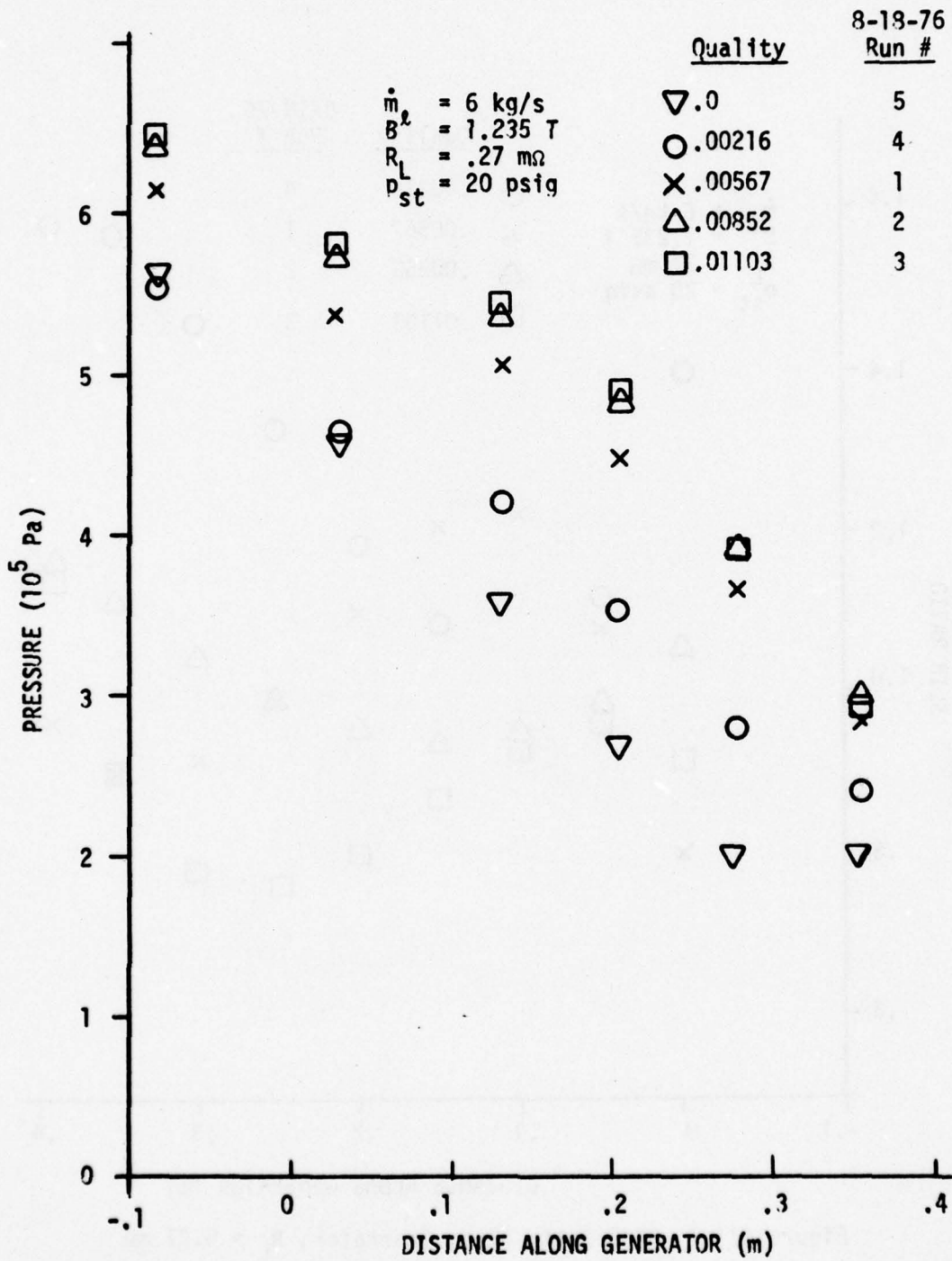


Figure III.8 Pressure Along Generator, $R_L = 0.27 \text{ m}\Omega$

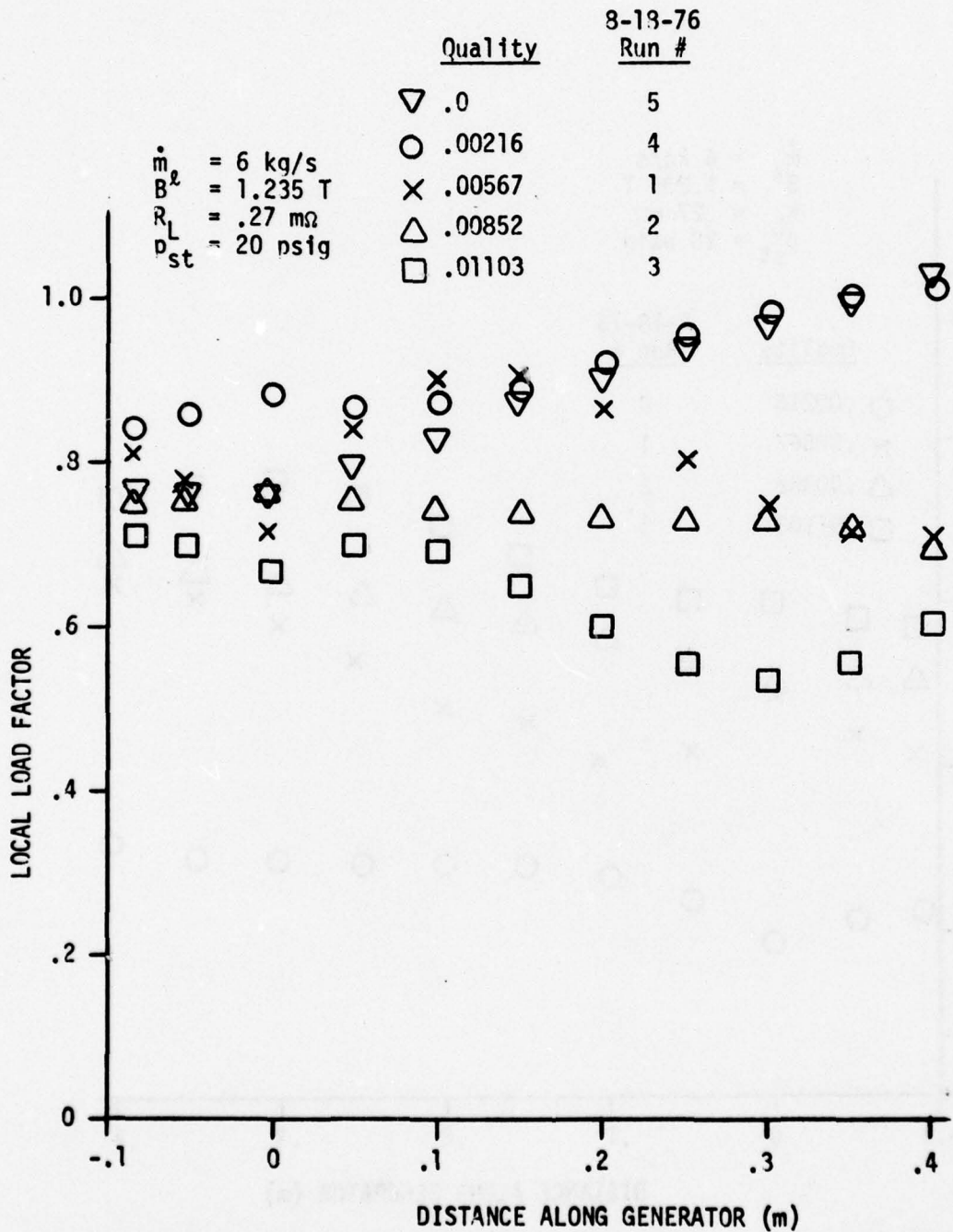


Figure III.9 Local Load Factor Along Generator, $R_L = 0.27 \text{ m}\Omega$

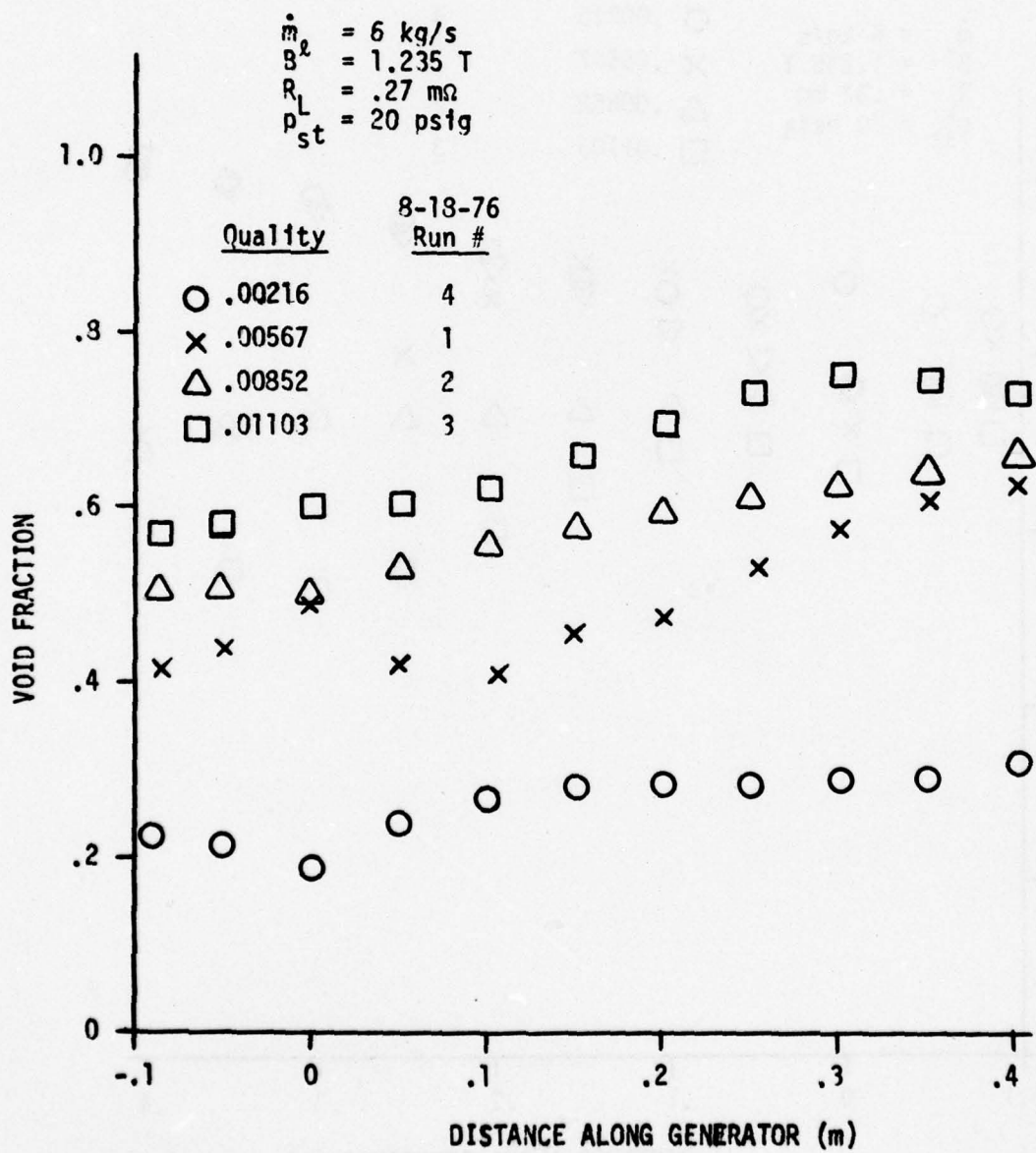


Figure III.10 Void Fraction Along Generator, $R_L = 0.27 \text{ m}\Omega$

fraction, probably due to the onset of entrainment of liquid droplets by the churning motion of the gas in the generator. The fact that the local slip ratio is less than unity at some point is not significant, this falls within the accuracy of the measurement.

III.2 Comparison of New and Old Runs

Sets of data with the old loop (7/7/75) and the revised loop immediately after construction (8/18/76 and 8/24/76) are listed in Table III.1. The efficiency as a function of quality was virtually unchanged, with the exception of the zero-quality runs (see below). However, as shown by the data for a quality of about 0.0058, the power level (pressure difference and voltage) was substantially higher (about 35% after correction for unequal magnetic fields) for the runs immediately after construction as compared to the runs with the old loop.

The runs with the highest power level (August 1976) had a lower measured average velocity slip ratio \bar{K} (ratio of gas to liquid velocity), implying that a more-uniform two-phase mixture existed in the generator, the liquid velocity was higher (higher voltage, current, and pressure drop), and the exit void fraction (ratio of gas volume to total volume) was larger. Also the fluctuation in the generator terminal voltage V_L was reduced, amounting to only a few percent of the average voltage. (Compare this with the previous runs.⁴)

The liquid velocities along the generator calculated from the measured void fractions and flow rates for the three runs at about 0.0058 quality are compared in Fig. III.11. Note that the differences in either the variations of or the average liquid velocities are not sufficient to account for the performance differences. An important difference is in the average load factor F , Table III.1. This is higher for the runs with the revised facility, indicating a higher

Table III.1

Comparison of Generator Data with Old and Revised Loops,
 $\dot{m}_g = 6 \text{ kg/s}$, Back Pressure = 0.14 MPa Gauge (20 psig)

Date	x	η_g [%]	B [T]	R_L [m Ω]	V_L [V]	Δp [0.1 MPa]	$\bar{\alpha}$	\bar{K}	\bar{F}
7/7/75 (old)	0	52.9	1.175	0.255	0.506	2.67	0	-	1.02
	0.00580	49.9	1.16	0.254	0.741	2.62	0.49	1.34	0.76
	0.00979	42.1	1.165	0.258	0.819	2.66	0.64	1.217	0.61
8/18/76 (revised)	0	39.4	1.253	0.26	0.470	3.01	0	-	0.89
	0.00216	48.1	1.24	0.27	0.665	3.31	0.27	1.272	0.93
	0.00567	50.3	1.235	0.27	0.867	3.75	0.49	1.047	0.82
	0.00852	46.4	1.238	0.27	0.932	3.90	0.59	1.007	0.74
	0.0110	43.1	1.235	0.27	1.01	4.16	0.68	0.876	0.62
8/24/76 (revised)	0	42.9	1.223	0.24	0.466	2.98	0	-	0.91
	0.00580	49.2	1.227	0.247	0.824	3.69	0.48	1.180	0.83
	0.00825	44.7	1.227	0.248	0.885	3.90	0.55	1.187	0.77
	0.01118	40.6	1.222	0.247	0.937	4.00	0.62	1.18	0.69
	0.0128	43.8	1.225	0.246	1.003	3.99	0.54	1.74	0.89

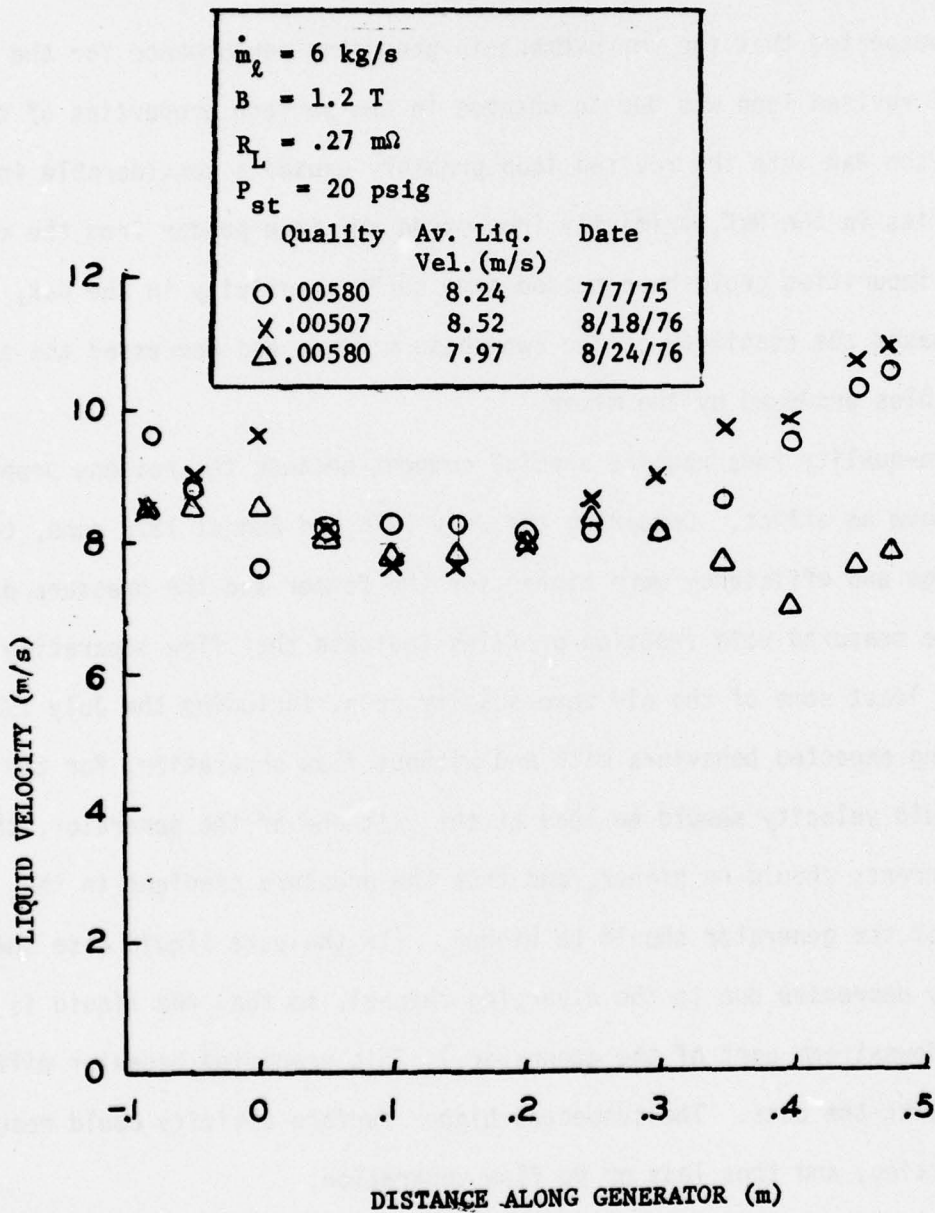


Figure III.11 Liquid Velocity Along Generator, 0.0058 Quality, Old and New Data

"effective" liquid velocity-electrical conductivity combination for the new runs. This result is expected from the reduced fluctuations.

It is suspected that the improvement in generator performance for the tests with the revised loop was due to changes in the surface properties of the NaK. Putting the NaK into the revised loop probably caused a considerable increase in the impurities in the NaK, primarily iron oxide and iron powder from the carbon steel. These impurities could have caused some surface activity in the NaK, and thus increased the stability of the two-phase mixture and decreased the size of the gas bubbles produced by the mixer.

The zero-quality runs require special comment because the reasons proposed above should have no effect. Comparing the July 1975 and August 1976 runs, the terminal voltage and efficiency were higher for the former and the pressure drop was lower. The measured void fraction profiles indicate that flow separation occurred in at least some of the old zero-quality runs, including the July 1975 case. Comparing expected behaviors with and without flow separation, for the latter the liquid velocity should be less at the exit end of the generator, the circulating currents should be higher, and thus the pressure gradient in the upstream part of the generator should be higher. (In the pure liquid case the liquid velocity decreases due to the diverging channel, so that the liquid is pumped in the downstream part of the generator.) This predicted behavior difference is consistent with the data. The suspected higher surface activity could result in improved wetting, and thus less or no flow separation.

The calculated performance from the generator prediction code is a terminal voltage of 0.477 V and an efficiency of 0.425 at 1.2 T, 6.0 kg/s pure NaK, and 0.25 m Ω load resistance. The August 1976 runs yielded values close to the calculated values.

III.3 Reduced Back Pressure

The liquid velocity, slip ratio, pressure, local load factor, and void fraction along the generator are shown in Figs. III.12 through III.16 for a back pressure only slightly above atmospheric pressure in the separator tank. In the old facility it was not possible to make runs with separator tank pressures below about 0.24 MPa absolute (35 psia) due to the high pressure drop between the separator tank and the suction side of the pump. With the improved piping system, the lower limit on separator tank pressure is that it be high enough to push the nitrogen through the six-inch line to the atmosphere.

A reduced generator back pressure means that higher volumetric flow rates and velocities are obtained in the generator with the same mass flow rate. Also, lowering the back pressure automatically increases the pressure ratio across the generator. This in turn means that the liquid velocity will be increasing along this generator since it was designed for a lower pressure ratio, and this should result in reduced generator performance.

The local load factor seems to show an increasing entrainment of liquid in the gas along the generator, Fig. III.15. The void fraction and slip ratio become quite large at the generator exit. The expected increase in the liquid velocity along the generator is observed for all of the non-zero quality runs, Fig. III.12.

A comparison of data for normal and reduced generator back pressures in Appendix A or Figs. III.6 and III.12 shows that the terminal voltage V_L is reduced for the lower-back-pressure runs even though the average liquid velocity is higher. The generator efficiencies for both back pressures are shown in Fig. III.17. The efficiency is lower for the lower back pressure, probably because of the varying velocity along the generator and thus increased circulating currents.

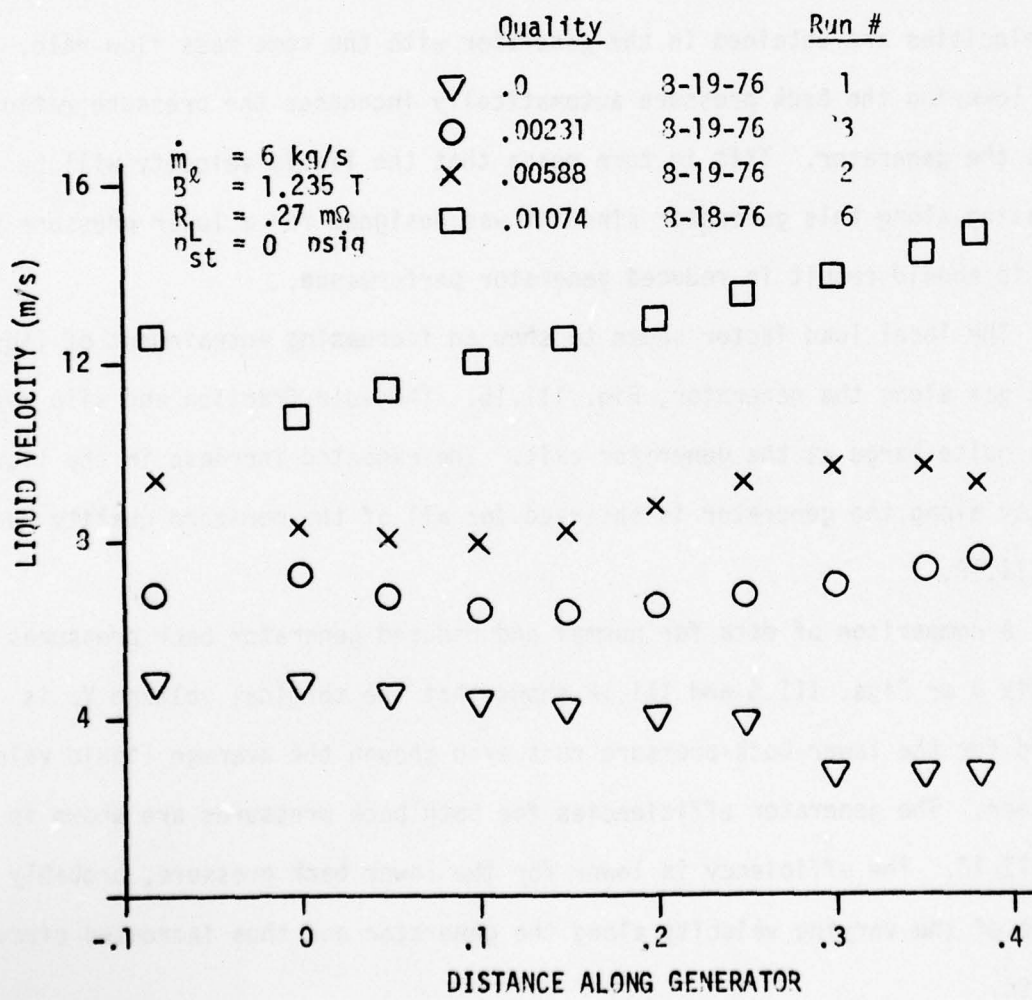


Figure III.12 Liquid Velocity Along Generator, Reduced p_{st}

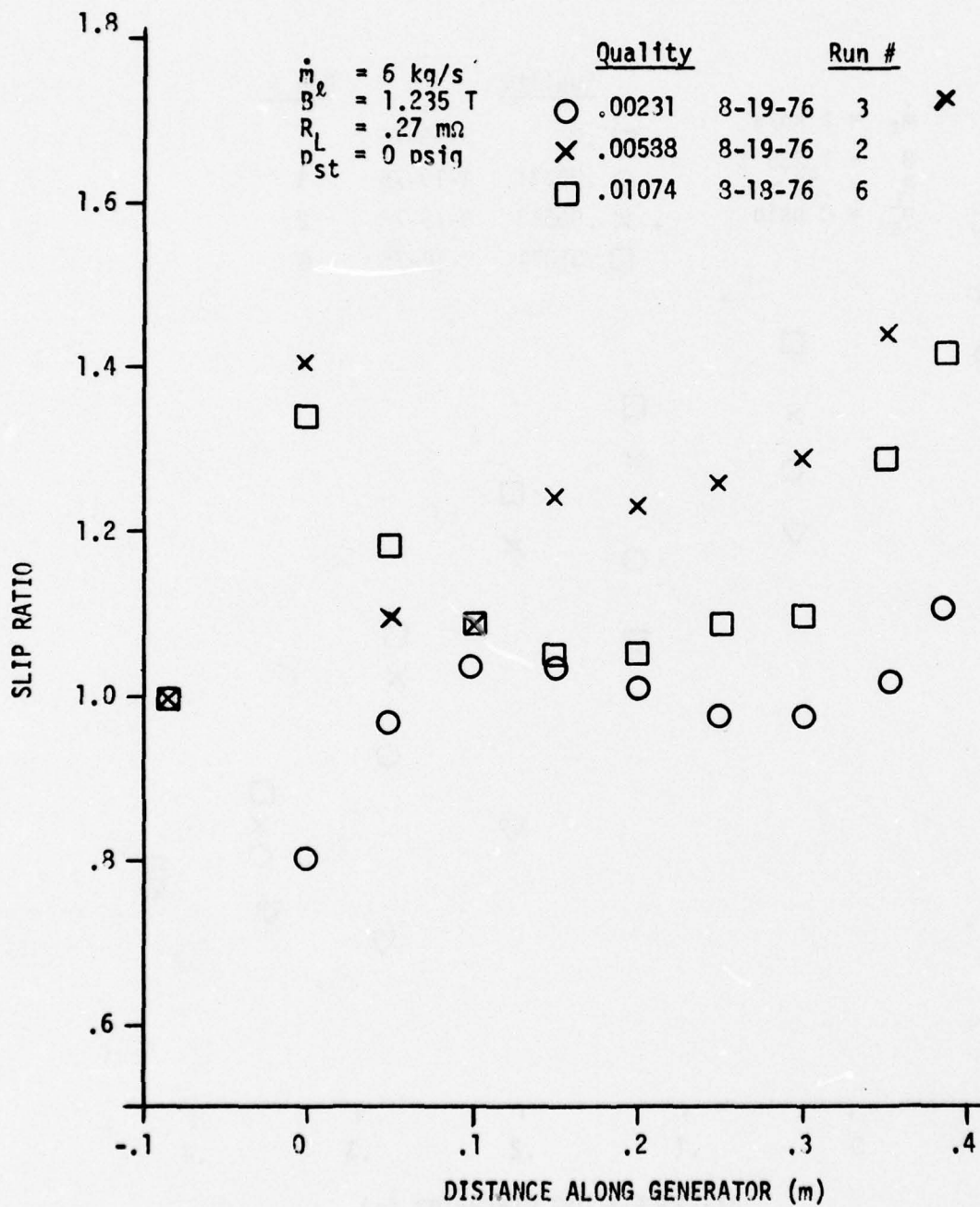


Figure III.13 Slip Ratio Along Generator, Reduced p_{st}

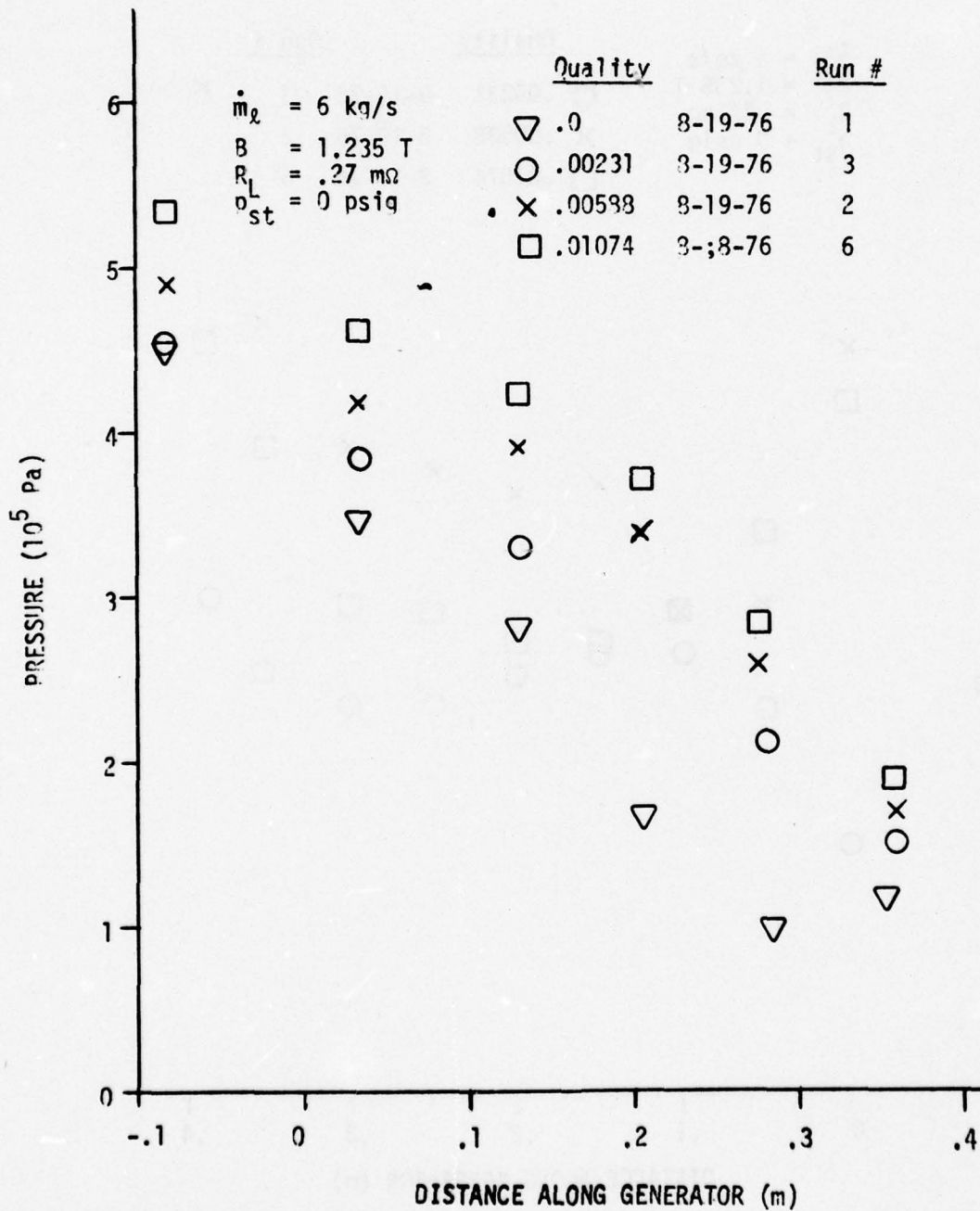


Figure III.14 Pressure Along Generator, Reduced p_{st}

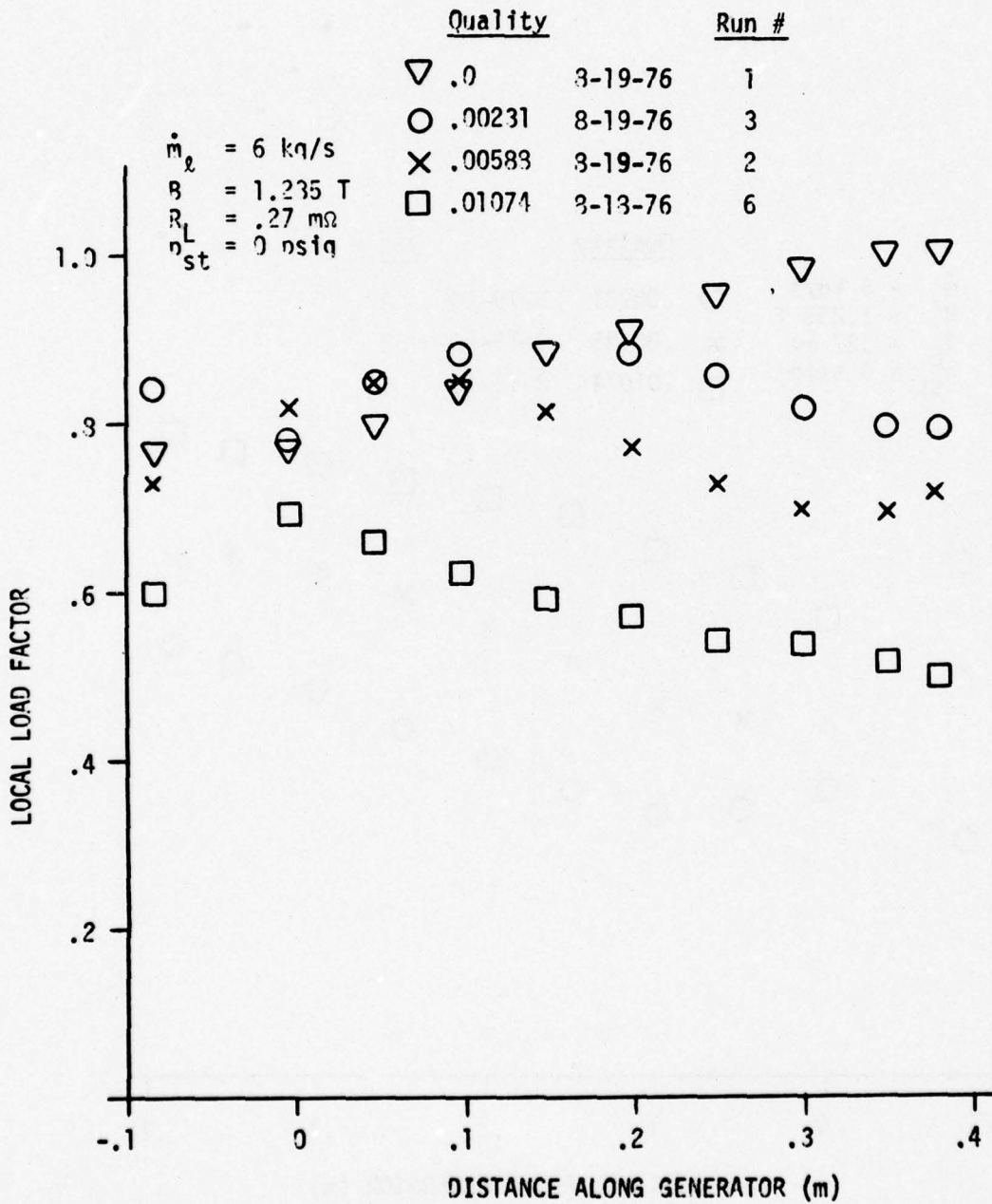


Figure III.15 Load Factor Along Generator, Reduced n_{st}

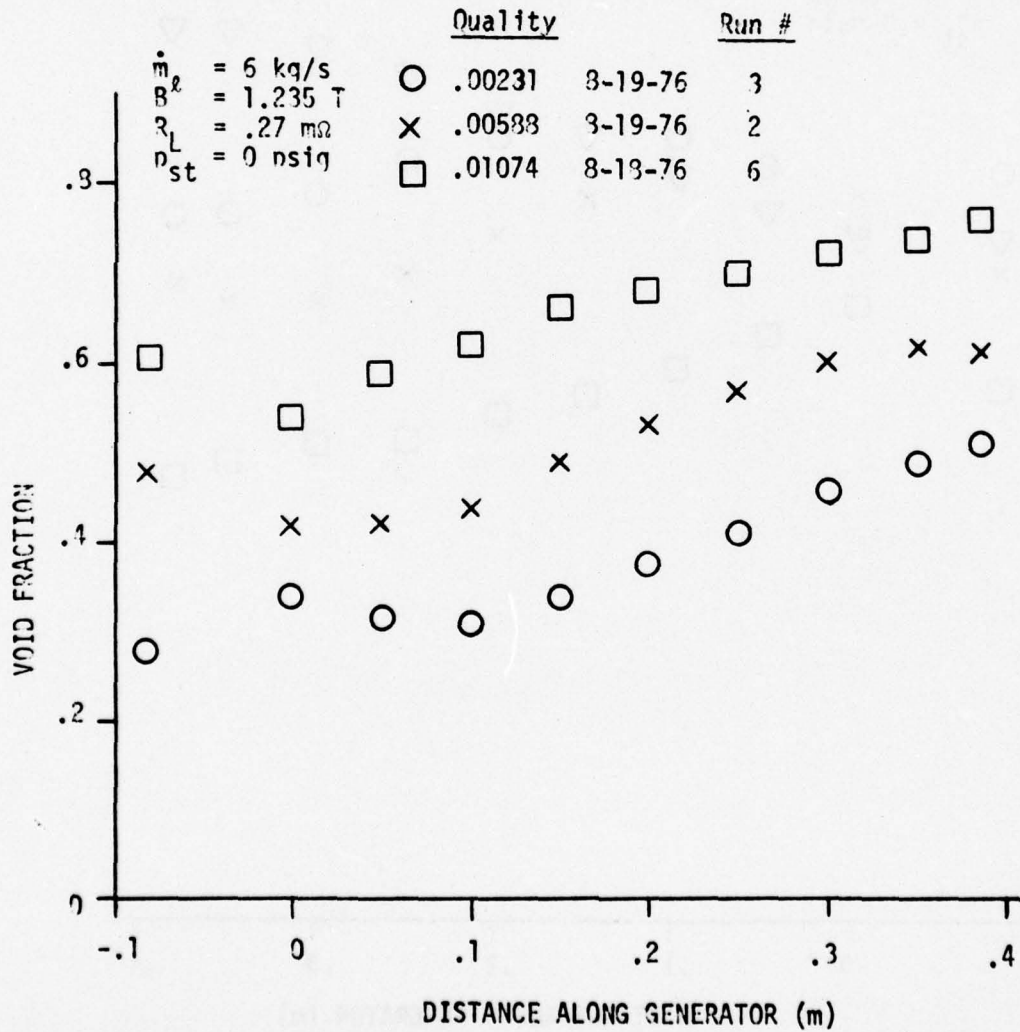


Figure III.16 Void Fraction Along Generator, Reduced p_{st}

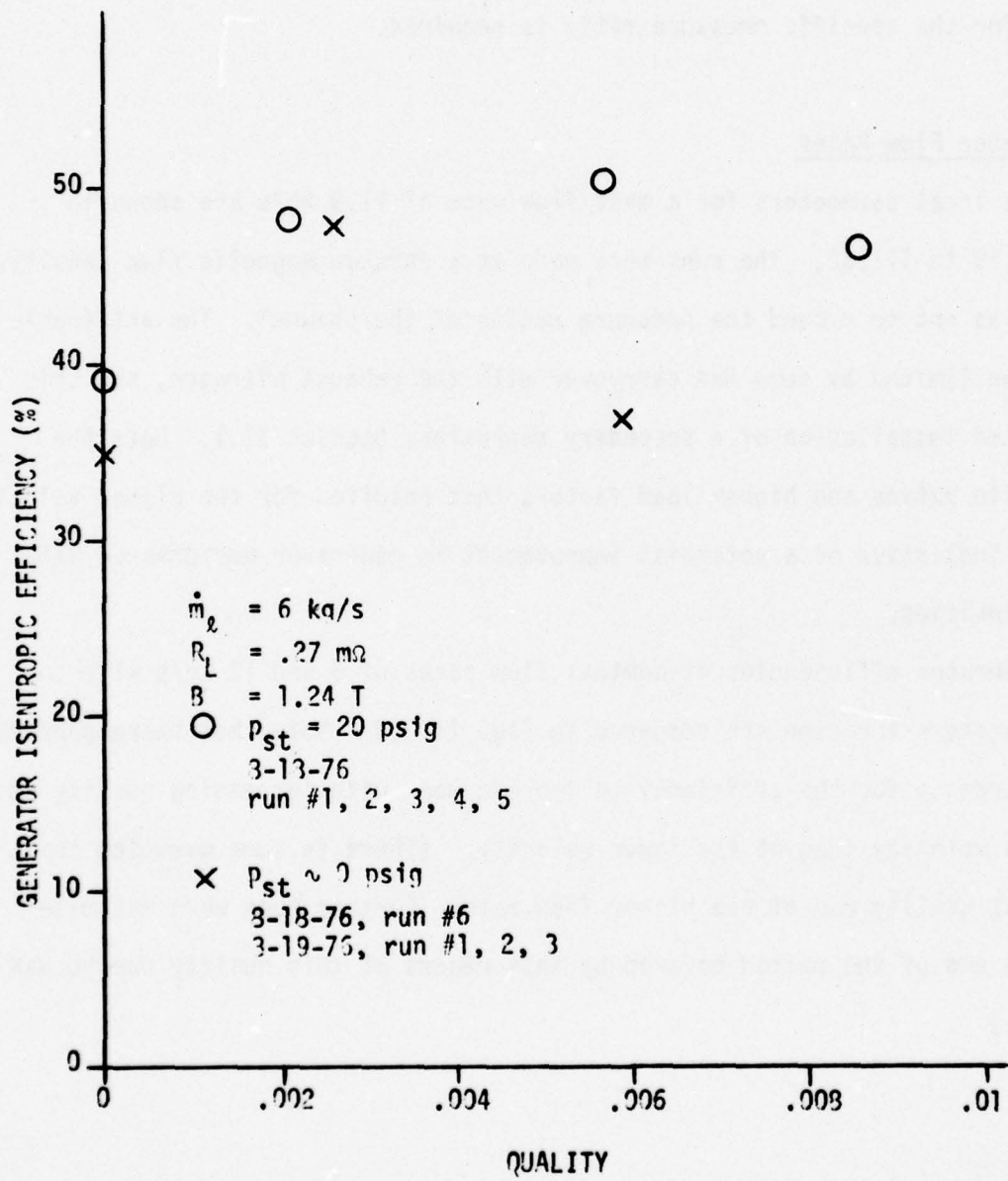


Figure III.17 Generator Isentropic Efficiency vs. Quality at Different Pressures in the Separation Tank

The ability to go to lower pressure at the generator exit will be useful in the future in obtaining larger pressure ratios across the generator, i.e., values closer to those anticipated for a commercial generator. Of course, to obtain high generator efficiency for higher pressure ratios a generator taper designed for the specific pressure ratio is required.

III.4 Higher Flow Rates

The local parameters for a mass flow rate of 11.9 kg/s are shown in Figs. III.18 to III.22. The runs were made at a reduced magnetic flux density, 0.6 T, so as not to exceed the pressure rating of the channel. The attainable quality was limited by some NaK carryover with the exhaust nitrogen, and this necessitated installation of a secondary separator, Section II.1. Note the reduced slip ratios and higher load factors that resulted for the higher velocity. These are indicative of a potential improvement in generator performance with higher velocities.

Generator efficiencies at nominal flow rates of 6 and 12 kg/s with the other parameters the same are compared in Fig. III.23. Note that there appears to be a tendency for the efficiency to improve more with increasing quality at the higher velocity than at the lower velocity. (There is some question about the highest quality run at the higher flow rate. Further runs were not made before the end of the period covered by this report at this quality due to NaK carryover.)

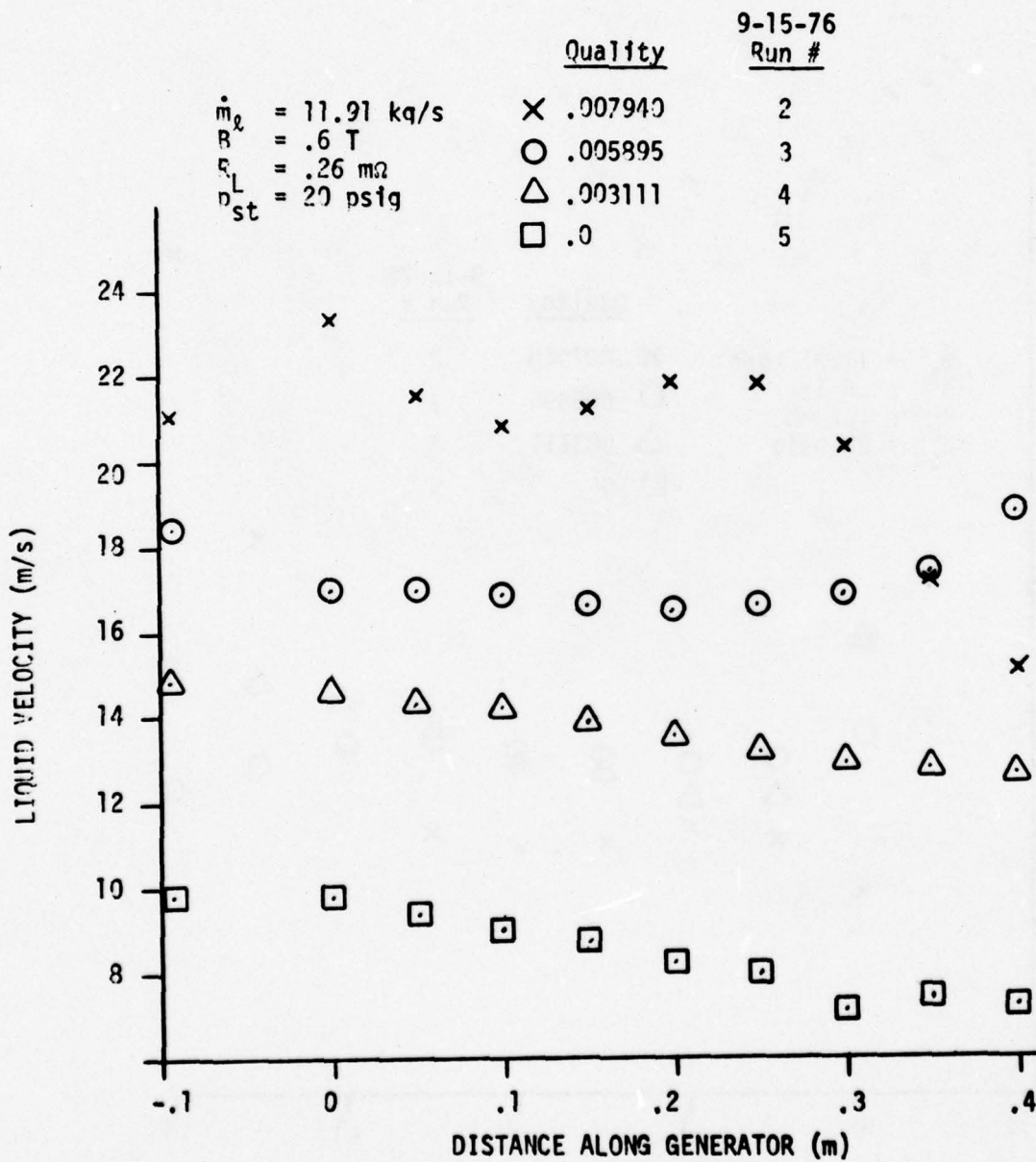


Figure III.18 Liquid Velocity Along Generator, $\dot{m}_L = 11.91$ kg/s

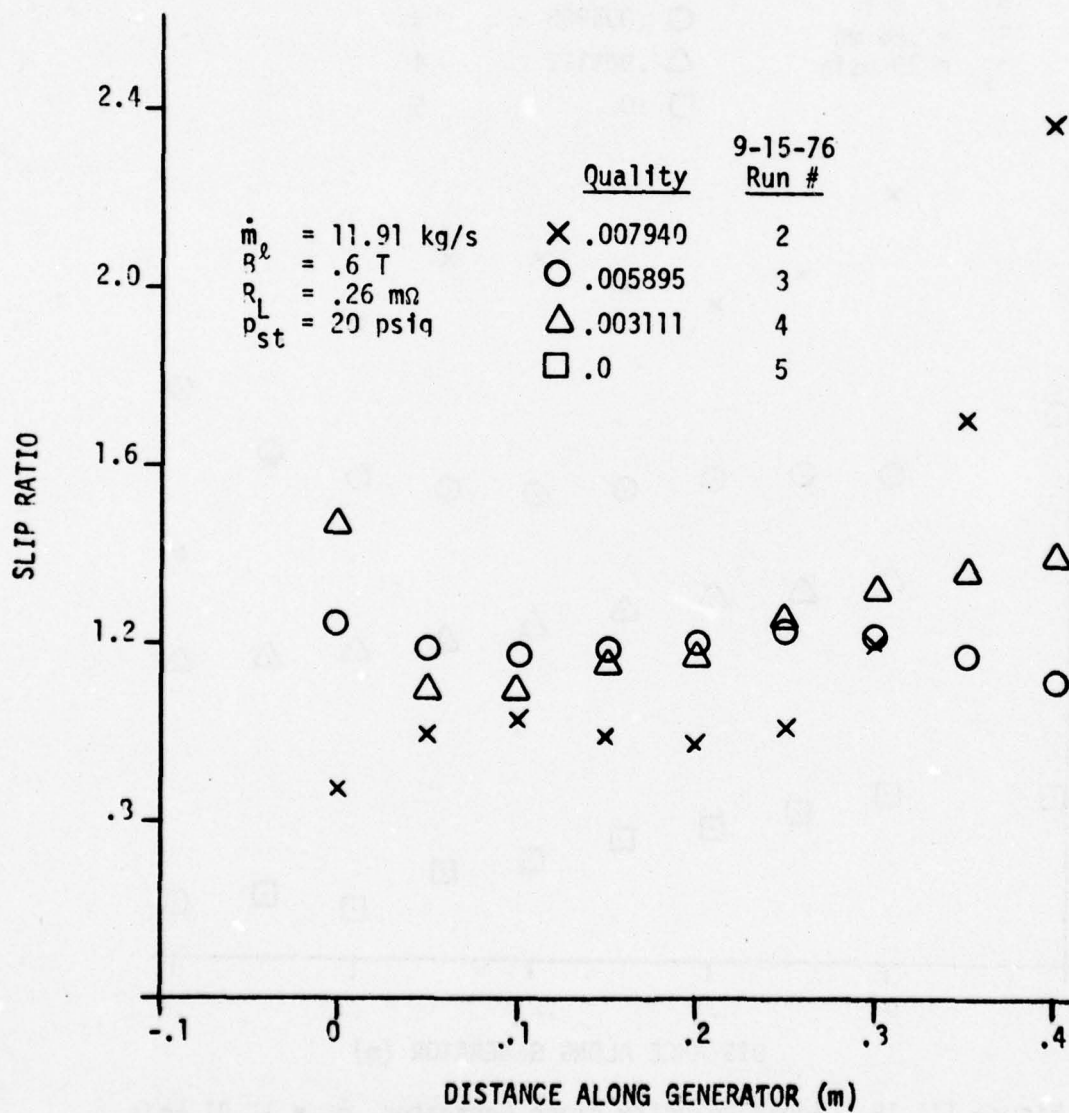


Figure III.19 Slip Ratio Along Generator, $\dot{m}_l = 11.91 \text{ kg/s}$

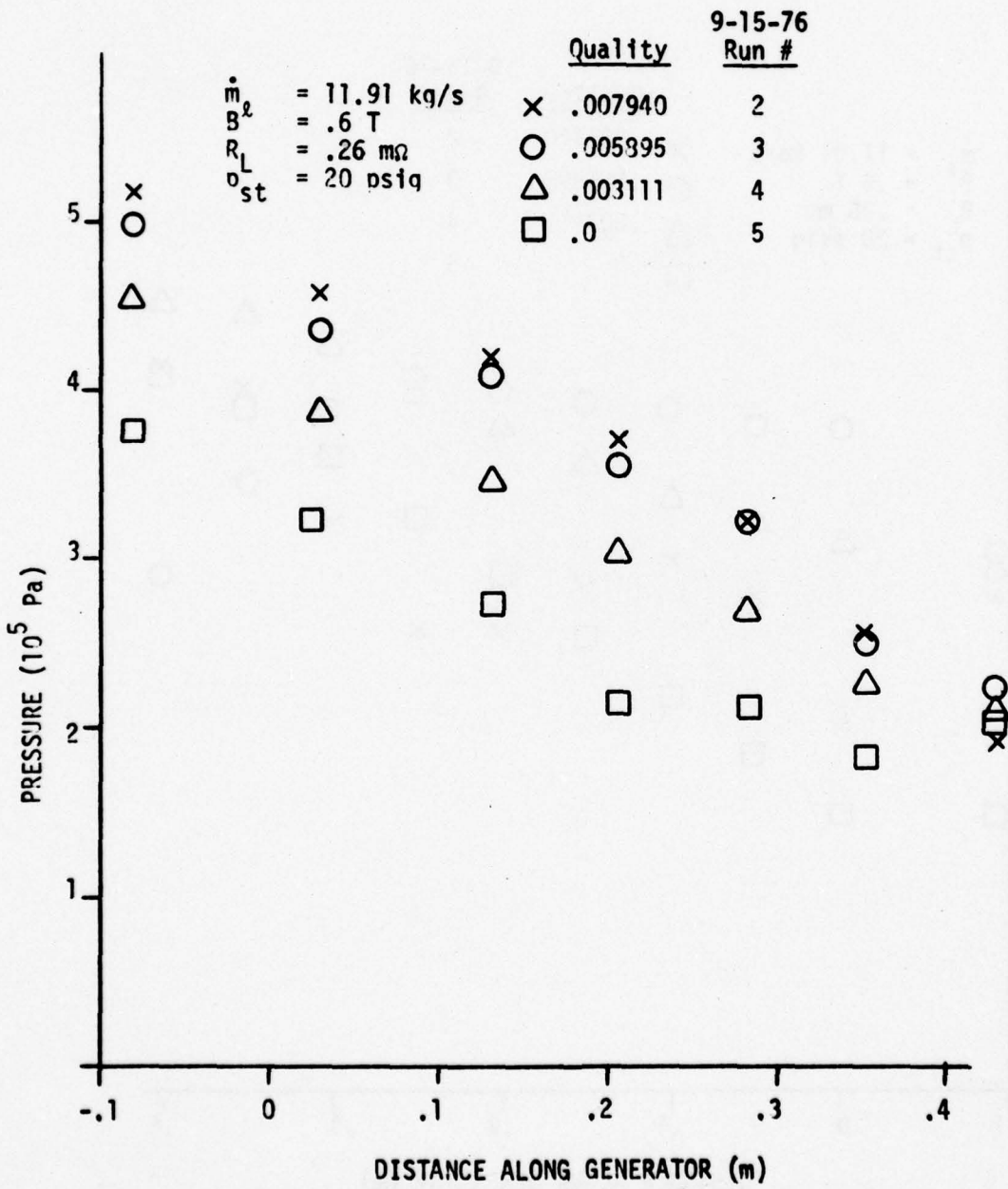


Figure III.20 Pressure Along Generator, $\dot{m}_e = 11.91 \text{ kg/s}$

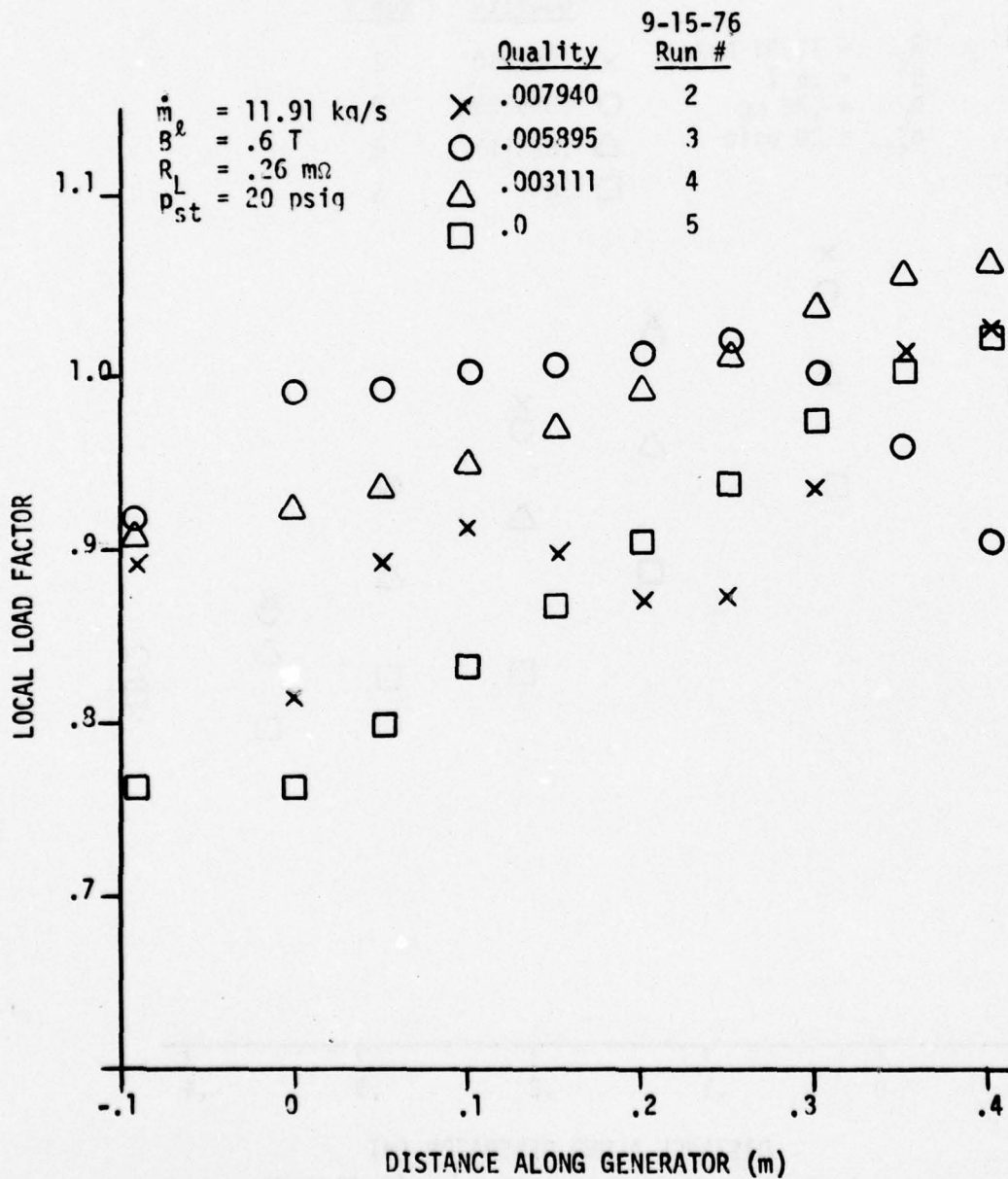


Figure III.21 Local Load Factor Along Generator, $\dot{m}_l = 11.91 \text{ kg/s}$

\dot{m}_2	= 11.91 kg/s	X	.007940	9-15-76
B_z	= .6 T	O	.005895	Run #
R_L	= .26 m Ω	Δ	.003111	
p_{st}	= 20 psig	\square	.0	

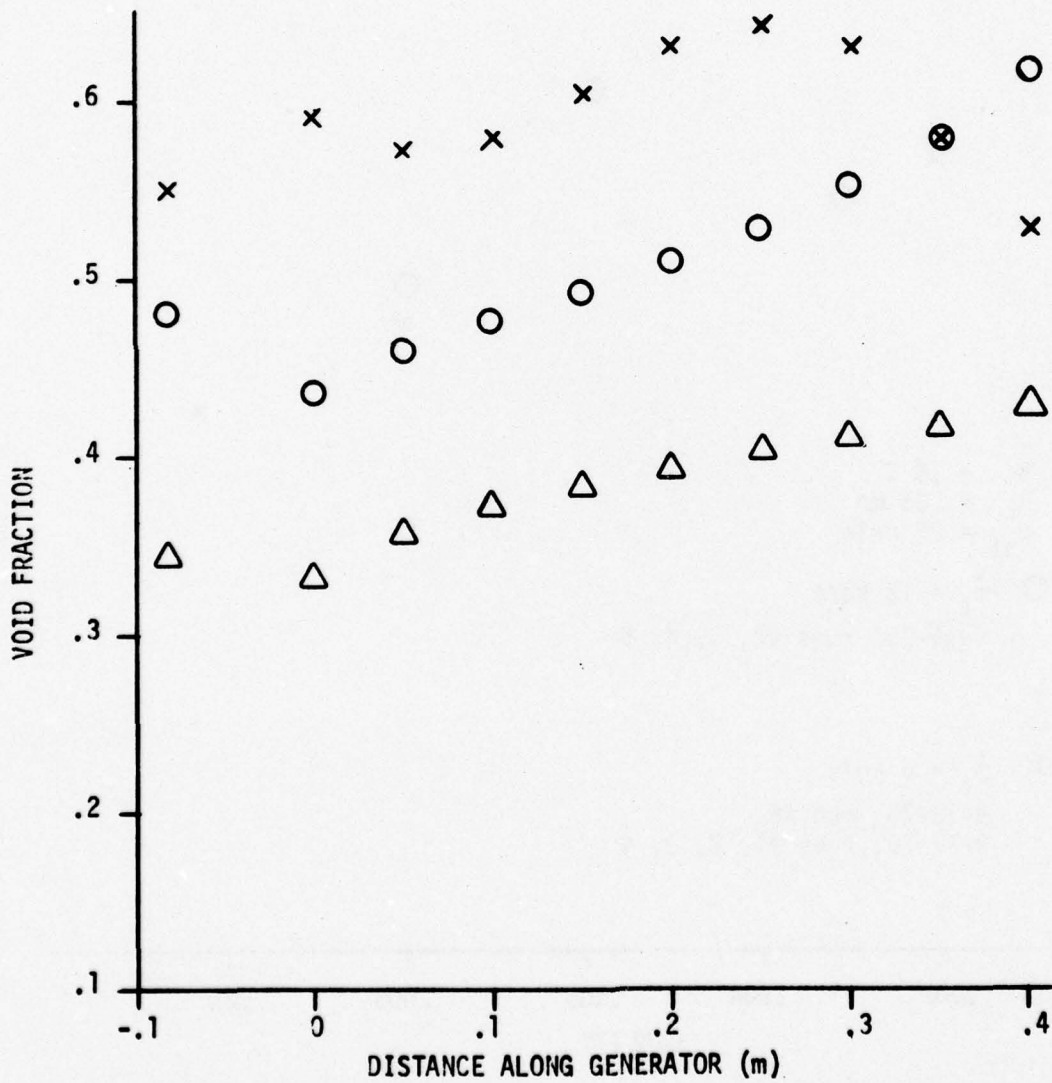


Figure III.22 Void Fraction Along Generator, $\dot{m}_2 = 11.91$ kg/s

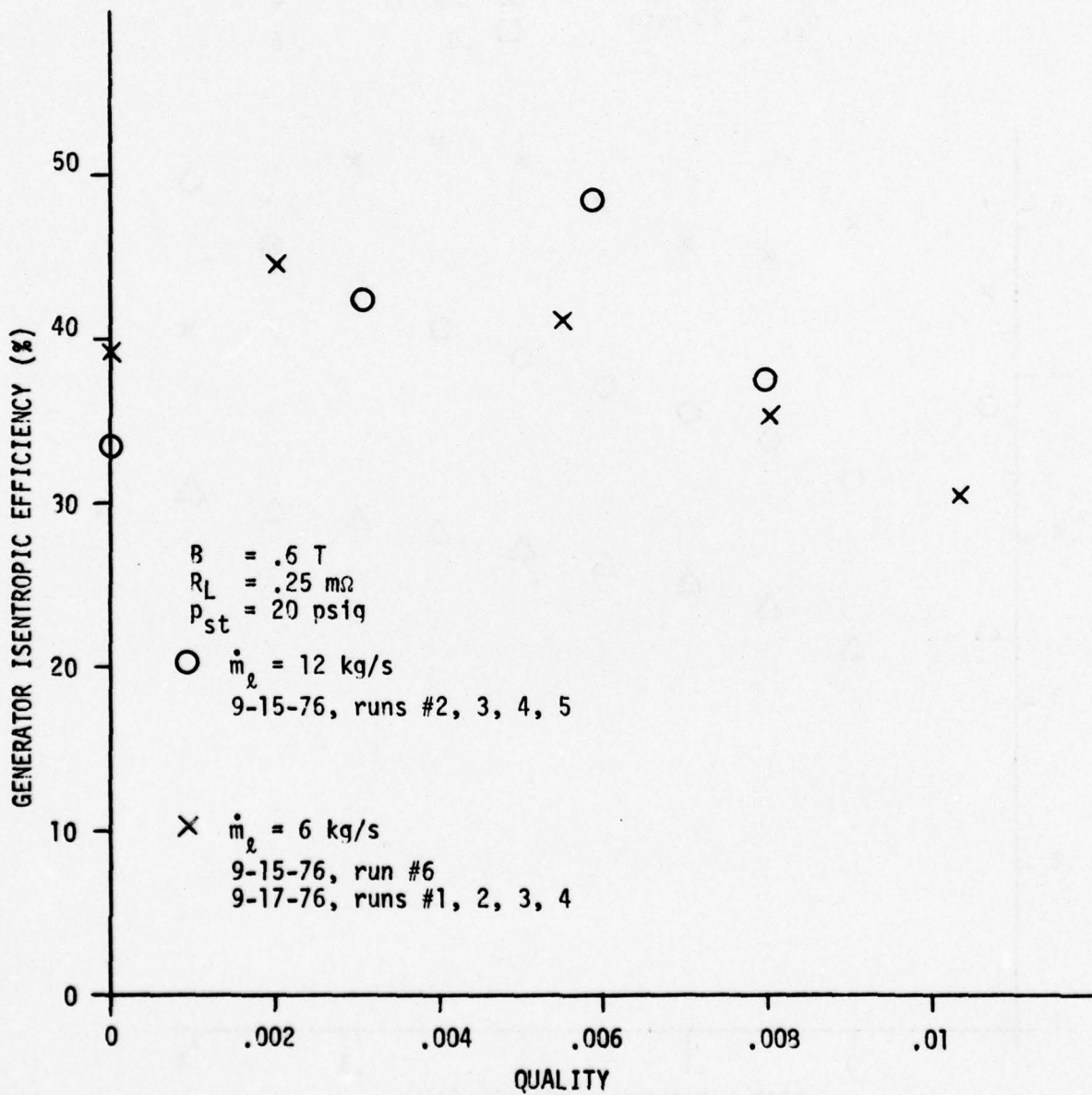


Figure III.23 Generator Isentropic Efficiency vs. Quality at Different Flow Rates

IV. ANALYTICAL STUDIES OF ANNULAR GENERATORS

IV.1 Introduction

Rectangular MHD conduction machine geometries for generators and liquid-metal pumps have been studied almost exclusively. Helical geometries are suitable for low-volume-flow-rate high-pressure difference pumps, but not for MHD generators. Annular geometries are common for induction pumps and generators, but there are no known references on annular conduction machines. Since the annular geometry has several advantages, the following analytical study was undertaken to evaluate its practicality.

The annular generator geometry considered consists of two concentric, homogeneous cylindrical walls of different radii with the conducting fluid flowing in the axial direction within the annulus, Fig. IV.1. Advantages of this geometry are:

1. The cylindrical walls are the electrodes, eliminating the need for insulating walls and the resulting fabrication problems. Without the insulating walls there are no accompanying viscous boundary layer and current shunting effects as found in rectangular geometries.

2. Homogeneous cylindrical shells are ideal pressure vessels.

3. The circumferentially-directed magnetic field is entirely contained within the generator, stray fields are not a problem, and the field is produced by a superconducting or ordinary torroidal winding without any magnetic iron.

Disadvantages of this geometry are:

1. The electrical terminal properties are inherently low voltage and high current because of the relatively-short electrode spacing and large cross-sectional area for current flow.

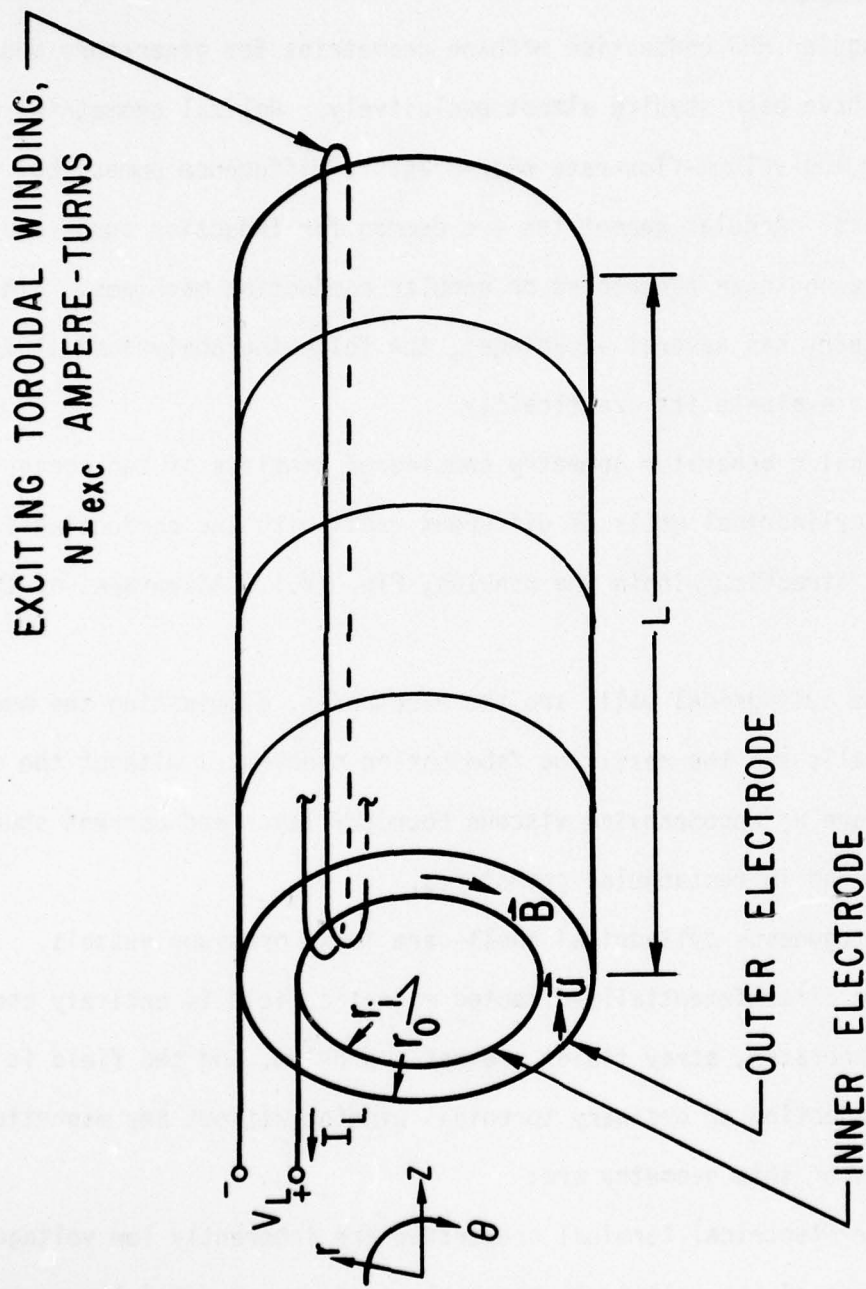


Figure IV.1 Annular Generator Geometry

2. The electromagnetic force density has an inverse-square radial dependence which may result in a very nonuniform velocity profile.

3. The magnetic field generated by the induced currents (armature reaction) may cause large variations in the power density along the machine, and there is no apparent method to compensate for this without destroying the first advantage.

4. The toroidal magnet winding has to be closed through the end regions of the annular duct, so that the wires must cross the flow area.

The first three disadvantages are analyzed in the following material by means of three simplified models. After establishing the relevant equations and assumptions, a model with a constant velocity and no armature reaction is considered to establish practical regions of operation in Section IV.3. A laminar velocity profile without armature reaction, Section IV.4, is used to study the effect of the inverse-square radial dependence of the electromagnetic force density. The flow in a practical generator could be either laminar or turbulent, depending on the relative laminarizing effect of the magnetic field, but the laminar solution yields insight into what might happen even for turbulent flow. Finally, the axial dependences of the magnetic flux and current densities for a constant fluid velocity are considered in Section IV.5. Numerical results obtained from an annular-geometry computer code are included for all three models. The primary objective of this study is generator operation, but the solutions apply equally to pump operation and numerical pump cases are also discussed. Only pure-liquid machines are considered, but the conclusions are valid for two-phase liquid-metal and plasma machines as well. The velocity-profile solution also has important implications for annular induction pumps and generators.

IV.2 Equations and Assumptions

All models considered are governed by the same general equations of fluid mechanics and electromagnetics. The assumptions made to solve the equations are:

1. Steady-state conditions,
2. Incompressible, Newtonian, non-polarizable fluid, i.e., pure liquid,
3. No fluid sources or sinks in the generator,
4. Negligible gravitational effects,
5. One-dimensional axial flow with circular symmetry about the axis of the cylindrical walls, and
6. The magnetic permeability is that of free space everywhere.

With these assumptions, the basic relevant equations are

$$\nabla \times \vec{B} = \mu_0 \vec{J}, \quad (\text{IV.1}) \quad (\text{IV.})$$

$$\vec{J} = \sigma(\vec{E} + \vec{u} \times \vec{B}), \quad (\text{IV.2})$$

$$\nabla \times \vec{E} = 0, \quad (\text{IV.3})$$

$$\nabla \cdot \vec{B} = 0, \quad (\text{IV.4})$$

$$\nabla \cdot \vec{u} = 0, \quad (\text{IV.5})$$

$$\text{and } \rho(\vec{u} \cdot \nabla)\vec{u} = -\nabla p + \mu \nabla^2 \vec{u} + \vec{J} \times \vec{B}; \quad (\text{IV.6})$$

where the variables are defined in the nomenclature.

In cylindrical coordinates with B_θ , u_z , J_r , and E_r as the only vector components the equations become

$$\frac{\partial}{\partial r} (rB_\theta) = 0, \quad (\text{IV.7})$$

$$-\frac{\partial B_\theta}{\partial z} = \mu_0 J_r, \quad (\text{IV.8})$$

$$J_r = \sigma(E_r - u_z B_\theta), \quad (IV.9)$$

$$\frac{\partial E_r}{\partial z} = 0 = \frac{\partial E_r}{\partial \theta}, \quad (IV.10)$$

$$\frac{\partial B_\theta}{\partial \theta} = 0, \quad (IV.11)$$

$$\frac{\partial u_z}{\partial z} = 0, \quad (IV.12)$$

and

$$\mu \left[\frac{\partial^2 u_z}{\partial r^2} + \frac{1}{r} \frac{\partial u_z}{\partial r} \right] = \frac{-\partial p}{\partial z} - J_r B_\theta. \quad (IV.13)$$

The magnetic flux density B_θ is most-easily determined from the integral form of Eq. IV.1 evaluated over a concentric circle about the axis, or

$$\oint_C \vec{B} \cdot d\vec{\ell} = 2\pi r B_\theta = \mu_0 \int_S \vec{J} \cdot \vec{n} da. \quad (IV.14)$$

For the applied field, the total field without armature reaction,

$$B_\theta = \frac{\mu_0 NI_{exc}}{2\pi r}, \quad (IV.15)$$

where NI_{exc} is the ampere-turns of the exciting toroidal winding, Fig. IV.1.

The electrical terminal properties, the electrode or load current I_L and the electrode voltage difference or load voltage V_L , are given by

$$I_L = -2\pi r \int_0^l J_r dz \quad (IV.16)$$

and

$$V_L = - \int_0^r E_r dr; \quad (IV.17)$$

where L is the length of the machine, and r_i and r_o are the radii of the inner and outer cylinders (electrodes).

The general equations for the powers are collected here for reference.

The ohmic loss in the fluid is

$$P_r = \int_{vol} \frac{J_r^2}{\sigma} r dr d\theta dz. \quad (IV.18)$$

The electrical output power with end loss neglected (negative for a pump) is

$$P_e = V_L I_L. \quad (IV.19)$$

The mechanical input power (negative for a pump) is

$$P_m = Q(\Delta p_{em} + \Delta p_v), \quad (IV.20)$$

where Q is the volumetric flow rate of the working fluid, Δp_{em} is the electromagnetic pressure difference,

$$\Delta p_v = \frac{f_p L u_z^2}{2D_h} \quad (IV.21)$$

is the (non-MHD) viscous pressure difference in terms of the Darcy friction factor f , and $D_h = 2(r_o - r_i)$ is the hydraulic diameter. The efficiencies for generator and pump operation are defined as

$$\eta_g \equiv \frac{P_e}{P_m} \quad \text{and} \quad \eta_p \equiv \frac{P_m}{P_e} \quad (IV.22)$$

It is convenient to use the normalized or non-dimensional radius

$$R \equiv r/r_i \quad (IV.23)$$

in the analysis. At the outer electrode,

$$R_o = r_o/r_i. \quad (IV.23a)$$

IV.3 Constant Velocity with no Armature Reaction

Constant fluid velocity with no armature reaction (the ideal case) is assumed to establish the parameters required for practical applications. The required equations are determined, and numerical examples calculated for both generator and pump operation.

IV.3.1 Analysis

The load or terminal current is

$$I_L = -2\pi r L J_r \quad (IV.24)$$

from Eq. IV.16. The terminal voltage is calculated from Eq. IV.17, where E_r is obtained by substituting I_L and B_θ from Eq. IV.15 into Eq. IV.9 and solving for E_r . The result is

$$V_L = \left[\frac{u_z \mu_o N I_{exc}}{2\pi} - \frac{I_L}{2\pi L \sigma} \right] \ln R_o \quad (IV.25)$$

in terms of the normalized radius. This can be interpreted as the equivalent circuit of Fig. IV.2, which has the equation

$$V_L = V_{oc} - I_L R_i \quad (IV.26)$$

The open-circuit voltage is

$$V_{oc} = \frac{u_z \mu_o N I_{exc} \ln R_o}{2\pi}, \quad (IV.27)$$

and the internal resistance is

$$R_i = \ln R_o / (2\pi L \sigma). \quad (IV.28)$$

In terms of the magnetic flux density at the inner radius, B_i , V_{oc} can be written as

$$V_{oc} = u_z B_i r_i \ln R_o. \quad (IV.27a)$$

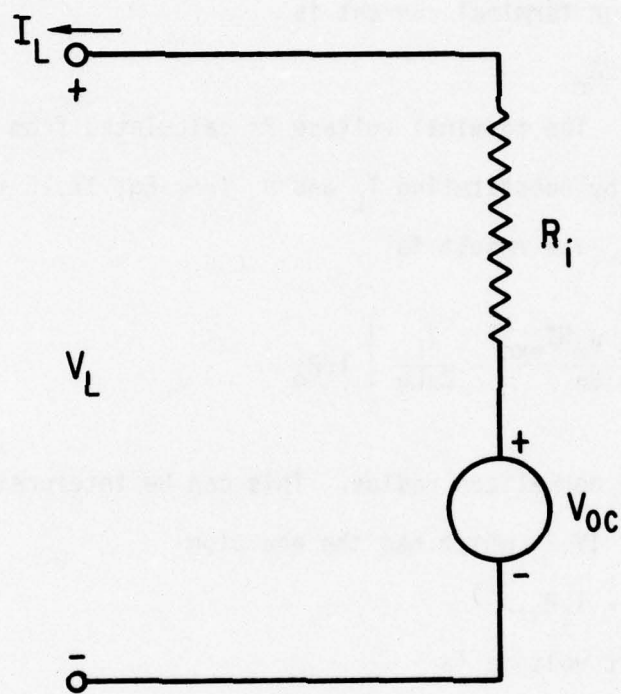


Figure IV.2 Equivalent Circuit

The ohmic power loss in the fluid, from Eq. IV.18, is

$$P_r = I_L^2 R_f. \quad (IV.29)$$

The electrical output power, Eq. IV.19, is written in terms of V_L as

$$P_e = \sigma L V_L (\mu u_z NI_{exc} - 2\pi V_L / \ln R_o) \quad (IV.30)$$

using Eq. IV.25 or Eq. IV.26 to eliminate I_L . In terms of the load factor, F , defined as

$$F = V_L / V_{oc}, \quad (IV.31)$$

Eqs. IV.29 and IV.30 can be written as

$$P_r = (V_{oc}^2 / R_f) (1 - F)^2 \quad (IV.29a)$$

and

$$P_e = (V_{oc}^2 / R_f) F(1 - F). \quad (IV.30a)$$

The calculation of P_m is more complicated because the electromagnetic pressure gradient is not constant over the channel cross section. To calculate Δp_{em} , the Lorentz force density $\vec{J} \times \vec{B}$ is integrated over the total channel volume, yielding

$$F_{em} = -\mu NI_{exc} I_L \ln R_o / 2\pi. \quad (IV.32)$$

The minus sign means that F_{em} acts in the $-z$ direction or opposes the fluid motion.

Then,

$$\Delta p_{em} = \frac{-F_{em}}{A} = \frac{\mu_o NI_{exc} I_L \ln R_o}{2\pi^2 r_f^2 (R_o^2 - 1)} \quad (IV.33)$$

is the average difference. The mechanical input power is calculated from Eqs. IV.20, IV.21, and IV.32, and the efficiency from Eq. IV.22. If the viscous pressure difference is negligible, then

$$P_m = (V_{oc}^2 / R_f) (1 - F) \quad (IV.34)$$

and

$$\eta_g = F \quad (IV.35)$$

as in rectangular MHD machines.

IV.3.2 Numerical Examples

The most significant parameter is the obtainable terminal voltage, as V_L must be large enough for either efficient dc to ac inversion or homopolar motors. Since the load factor F must be close to unity for efficient generator or pump operation, Eq. IV.35, V_{oc} is given in Table IV.1 for values of r_1 , R_0 , B_1 , and u_z . Note that R_0 is limited to be much less than 1.1 at reasonable power densities to prevent the possibility of flow reversal, as shown in Section IV.4. The velocity is limited to around 25 to 50 m/s by viscous loss. None of the cases shown yields adequate voltage, even at $B_1 = 6$ T and $r_1 = 5$ m. Higher voltages are obtainable with several generators connected electrically in series, except that the output power per generator (see Table IV.2) may be too large to use several generators in one power plant.

The powers are shown in Tables IV.2 as a function of the load factor F for one of the cases from Table IV.1. For an acceptable efficiency with all losses included (end losses are ignored here) F will most likely be between 0.9 and 0.95, leading to a generator power on the order of 500 MW per meter of length and V_L around 7 V at $r_1 = 1$ m and $B_1 = 3$ T. Since the power scales as V_{oc}^2 (or r_1^2 or B_1^2) at constant R_0 and F , Eq. IV.30a, increasing V_{oc} results in increased P_e and no possibility of a series connection to raise the useable voltage. Finding a good compromise between generator size, power level, and terminal voltage is very difficult for a rectangular generator, and still more difficult, if not impossible, for large annular generators.

There are no applications for electromagnetic pumps of the power levels shown in Table IV.2. Thus, acceptable voltage levels may be unattainable for annular conduction pumps since the size and voltage must be reduced from the values of Table IV.2. The low voltages shown in Table IV.2 are not surprising, they result from the relatively-short electrode spacing mentioned in Section IV.1.

Table IV.1

Open-Circuit Voltage and Excitation Ampere-Turns as a Function of Electrode Radii, Magnetic Field Strength at r_1 , and Constant Velocity

r_1 [m]	R_0	B_1 [T]	u_z [m/s]	NI_{exc} [10^7 AT]	V_{oc} [V]
1	1.1	3	25	1.5	7.15
1	1.1	3	50	1.5	14.3
1	1.1	6	25	3.0	14.3
1	1.2	3	25	1.3	13.7
3	1.1	3	25	4.5	21.4
3	1.01	3	25	4.5	2.24
3	1.1	6	25	9.0	42.9
3	1.2	3	25	4.5	27.3
5	1.1	3	25	7.5	35.7
5	1.01	3	25	7.5	3.73
5	1.1	6	25	15.0	71.5
5	1.1	3	50	7.5	71.5
5	1.2	3	25	7.5	68.4

Table IV.2

Powers per Meter Length for $r_i = 1$ m, $R_o = 1.1$, and Constant Velocity

Fluid = NaK
 $B_i = 3$ T
 $u_z = 25$ m/s
 $NI_{exc} = 1.5 \times 10^7$ AT
 $V_{oc} = 7.15$ V

$\rho = 867$ kg/m³
 $\sigma = 2.62 \times 10^6$ mhos/m
 $D_h = 0.2$
 $f^h = 0.022$
 $R_m = 82.3$

	F	V_L [V]	I_L [MA]	P_e [MW]	P_m [MW]	Useful Power Density [MW/m ³]	η_g [%]
Gen.	0.8	5.72	247	1410	1770	2140	79.9
Gen.	0.95	6.79	61.8	420	442	636	94.9
Pump	1.1	7.86	-123	-971	-882	1340	90.9
Pump	1.3	9.29	-370	-3440	-2650	4010	76.9

IV.4 Fully-Developed Laminar Flow with no Armature Reaction

In this section the effect of the radial dependence of the electromagnetic force density is analyzed. Fully-developed laminar flow is treated because analytical solutions can be obtained. The laminar-flow solution provides a guide for the behavior of turbulent flows.

IV.4.1 Analysis

First the velocity profile $u_z(r)$ must be determined. The electromagnetic force density $J_r B_\theta$ can be written as

$$J_r B_\theta = - \frac{\mu_o N I_{exc} I_L}{(2\pi r)^2 L} = \frac{-r_i B_i I_L}{2\pi r^2 L} \quad (IV.36)$$

from Eqs. IV.15 and IV.24. The pressure gradient can be expressed as $\partial p / \partial z = -\Delta p / L$, where Δp equals the inlet minus the exit pressures. Note that Δp is independent of r and z for fully-developed flow and is positive for generator operation. Substituting into Eq. IV.13 and solving for $u_z(r)$ with the boundary conditions that $u_z = 0$ at the walls yields

$$u_z(R) = [-\ln R \ln(R_o/R)] \frac{r_i B_i I_L}{4\pi L \mu} + \left[\frac{R_o^2 - 1}{\ln R_o} \ln R - (R^2 - 1) \right] \frac{r_i^2 \Delta p}{4L\mu} \quad (IV.37)$$

in terms of the normalized radius R . Note that this is not a Hartmann profile, and there is no parameter like the Hartmann number governing the shape of the velocity profile.

Next V_L is calculated using the same procedure as in Section IV.3.1 except that $u_z(R)$ is given by Eq. IV.37. The result, in terms of the equivalent circuit of Fig. IV.2 or Eq. IV.26, is

$$V_{oc} = [R_o^2(\ln R_o - 1) + 1 + \ln R_o] \frac{r_i^3 B_f \Delta p}{8L\mu} \quad (IV.38)$$

and

$$R_i = \left[\frac{\ln R_o}{2\pi L\sigma} + \frac{r_i^2 B_f^2 (\ln R_o)^3}{24\pi L\mu} \right]. \quad (IV.39)$$

Note that R_i is not the physical internal resistance $\ln R_o / 2\pi L\sigma$. The second term, which is independent of σ , comes from the specified constant pressure difference. With Δp fixed, the average fluid velocity or the volume flow rate Q decreases as I_L increases because of the increased (adverse) electromagnetic pressure gradient. In Section IV.3.1, on the other hand, u_z (or Q) was specified and Δp had to increase with increasing I_L .

The ohmic power loss is still given by Eq. IV.29 since the second term of Eq. IV.39 does not represent a physical resistance. The electrical output power $P_e = V_L I_L$ is expressed as a function of Δp and I_L using Eqs. IV.26, IV.38, and IV.39. The mechanical input power is calculated from $P_m = Q\Delta p$, where the volumetric flow rate is

$$Q = \int_{r_i}^{r_o} 2\pi r u_z dr. \quad (IV.40)$$

Integrating Eq. IV.40 using Eq. IV.37 results in

$$P_m = [R_o^2(\ln R_o - 1) + 1 + \ln R_o] \frac{r_i^3 B_f I_L \Delta p}{8L\mu} + \left[\frac{R_o^2 - 1}{\ln R_o} - (R_o^2 + 1) \right] \frac{\pi r_i^4 (R_o^2 - 1) \Delta p^2}{8L\mu}. \quad (IV.41)$$

The viscous power dissipation can be calculated from

$$P_v = 2\pi L \int_{r_i}^{r_o} \mu \left(\frac{\partial u_z}{\partial r} \right)^2 r dr \quad (\text{IV.42})$$

using Eq. IV.37, or from the other powers and conservation of energy.

IV.4.2 Numerical Examples

The velocity profiles for $r_i = 3$ m, $R_o = 1.01$, $B_i = 3$ T, $V_L = 4$ V, NaK, and three pressure gradients are shown in Fig. IV.3. The powers for these parameters and six pressure gradients, including the three plotted in Fig. IV.3, are given in Table IV.3. Increasing pressure gradient corresponds to decreasing load factor F , as shown in Table IV.3. Note that for small pressure gradients (F close to unity) the profile resembles the non-electromagnetic annular profile, the viscous and ohmic losses are small, and the power density is low. At a power density of about 30 MW/m³ flow reversal occurs (Fig. IV.3) and the viscous power loss is substantial. Although the efficiency is very high, the load factor is so close to unity that the power density is relatively low for practical MHD generators and the end losses (not included) would be serious.

A similar behavior is observed for $R_o = 1.1$, Fig. IV.4, except that the flow reversal occurs at a lower pressure gradient or power density because of the larger variation in the electromagnetic pressure gradient across the channel cross section.

Note that the behavior of the annular generator is different from the conventional rectangular generator in that flow reversal occurs and the viscous losses increase sharply with generator loading (decreasing F). Flow reversal occurs for all cases except very low power densities so that the viscous contribution to the total pressure gradient can balance out the radial variation of the electromagnetic pressure gradient. In the rectangular generator

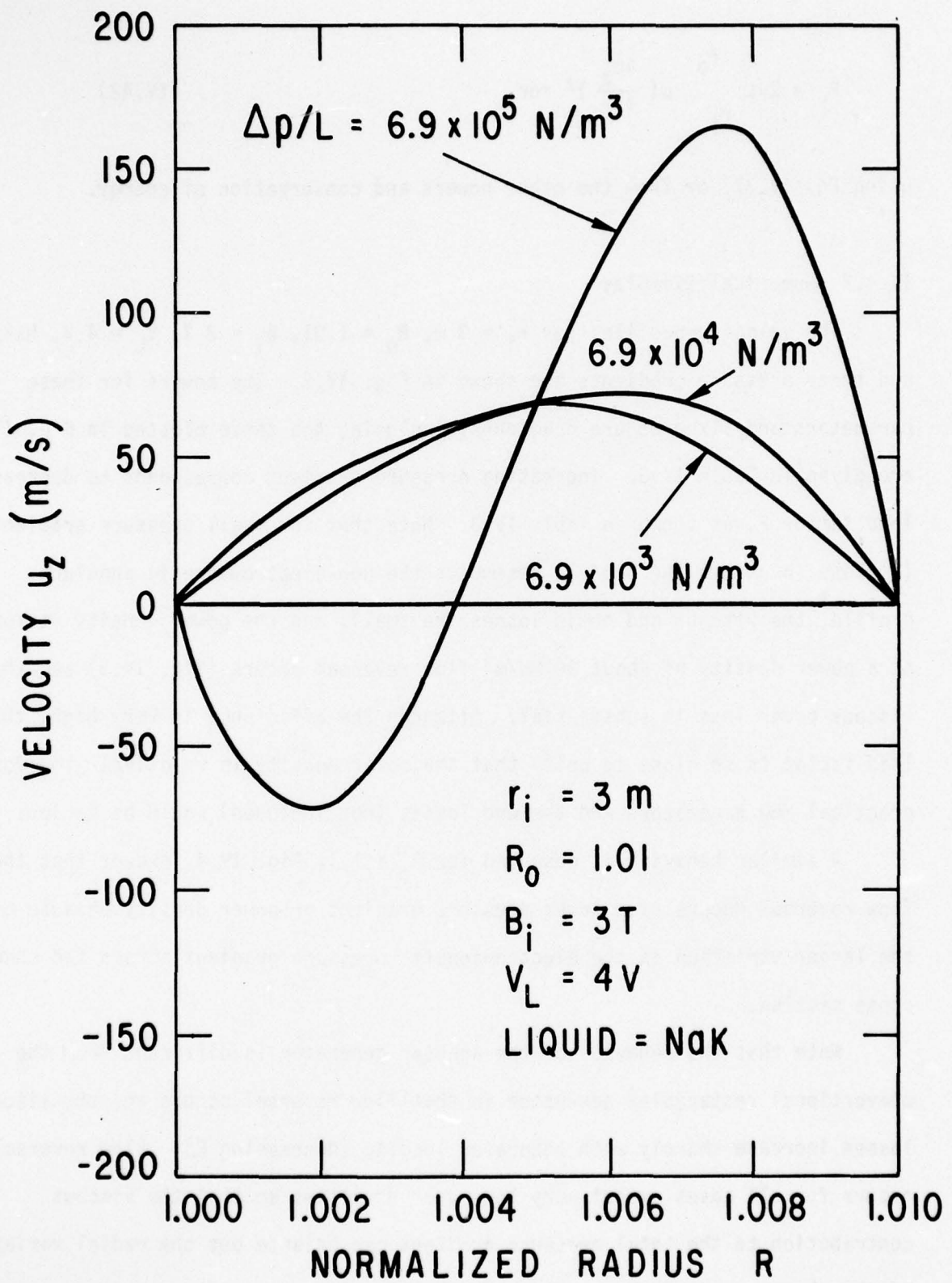


Figure IV.3 Velocity Versus Radius as a Function of the Pressure Gradient, $R_0 = 1.01$

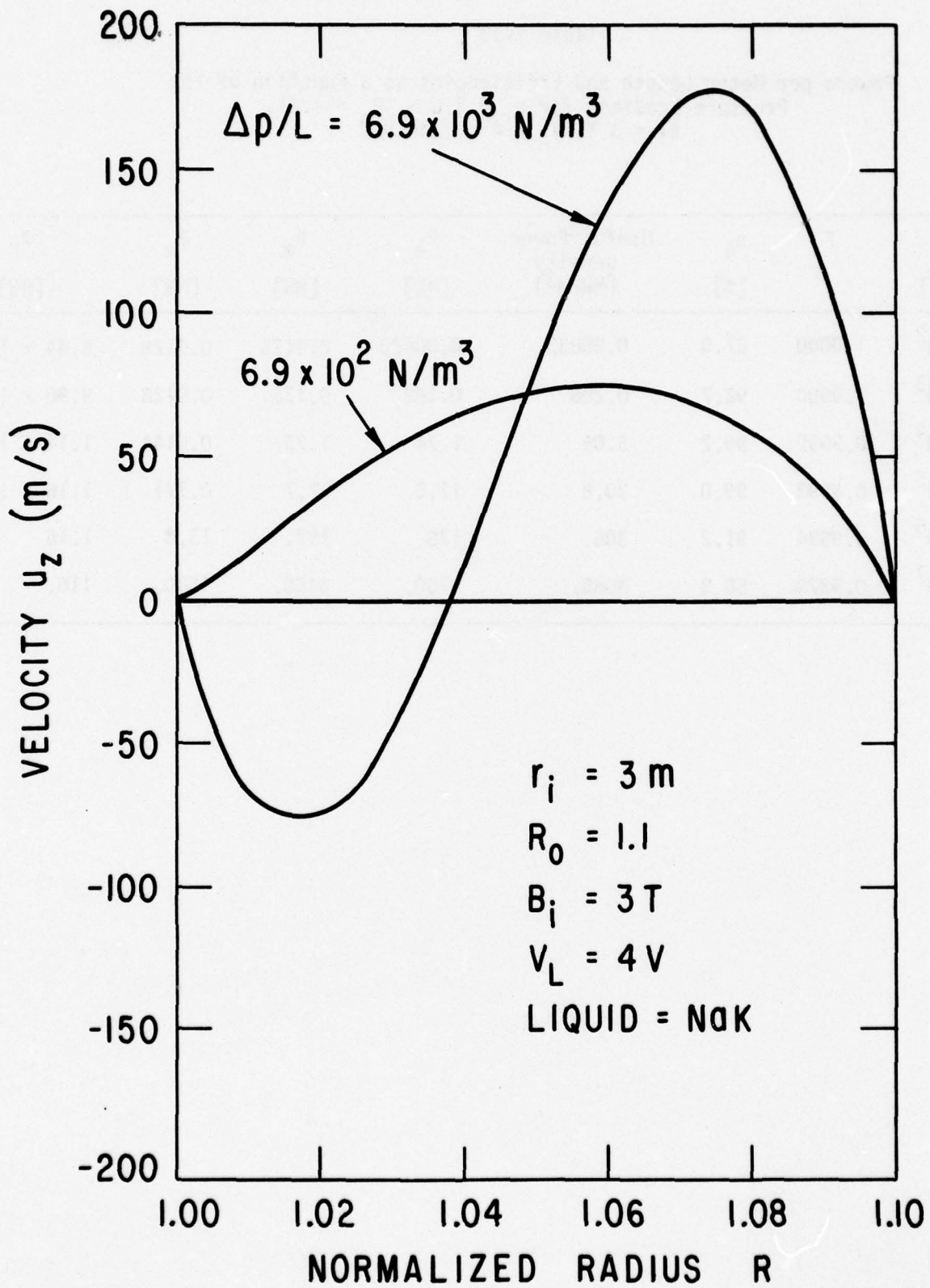


Figure IV.4 Velocity Versus Radius as a Function of Pressure Gradient, $R_0 = 1.1$

Table IV.3

Powers per Meter Length and Efficiencies as a Function of the
 Pressure Gradient for $r_i = 3.0$ m, $R_o = 1.01$,
 $B_i = 3$ T, $V_L = 14$ V, and NaK

$\Delta p/L$ [N/m ³]	F	η_g [%]	Useful Power Density [MW/m ³]	P_e [MW]	P_m [MW]	P_v [MW]	P_r [MW]
6.9×10^2	1.0000	27.0	0.00832	0.00473	0.0175	0.0128	8.44×10^{-10}
6.9×10^3	1.0000	92.7	0.286	0.162	0.175	0.0128	9.96×10^{-7}
6.9×10^4	0.9999	99.2	3.06	1.74	1.75	0.0144	1.14×10^{-4}
6.9×10^5	0.9993	99.0	30.8	17.5	17.7	0.171	1.16×10^{-2}
6.9×10^6	0.9934	91.2	308.	175.	192.	15.8	1.16
6.9×10^7	0.9379	50.8	3080.	1750.	3450.	1580.	116.

viscous power loss is almost constant, except for the slight increase in average velocity needed to hold the load voltage constant as F is decreased. In the cases considered for the annular generator the viscous loss is always much larger than the ohmic loss, and the efficiency decrease at higher power density (lower F) is caused by the sharp increase in the viscous loss with the flow reversal and the resulting large shear forces.

The velocity profiles for two sets of pump cases, $R_0 = 1.01$ and 1.1 , are shown in Figs. IV.5 and IV.6, respectively. The corresponding powers and efficiencies are given in Tables IV.4 and IV.5. In both cases flow reversal occurs, although at a much higher pressure gradient or power density for the $R_0 = 1.01$ case because of the smaller change in the electromagnetic force density across the channel. Note that for even higher pressure gradients or power densities the devices become dissipators, absorbing both electrical and mechanical input powers and dissipating them as ohmic and viscous losses. (A similar effect will occur with any pump. A pump has a given pressure difference with zero flow; if a higher pressure difference is imposed, then reversal of the net flow will occur.)

The voltage levels for the pump cases are very low because of the short electrode spacing. Both cases considered have the same average electric-field strength. The low voltages mean that the device is probably not practical.

The results obtained here are only valid for laminar flows. However, similar effects are expected with turbulent flows, including flow reversal at high power densities.

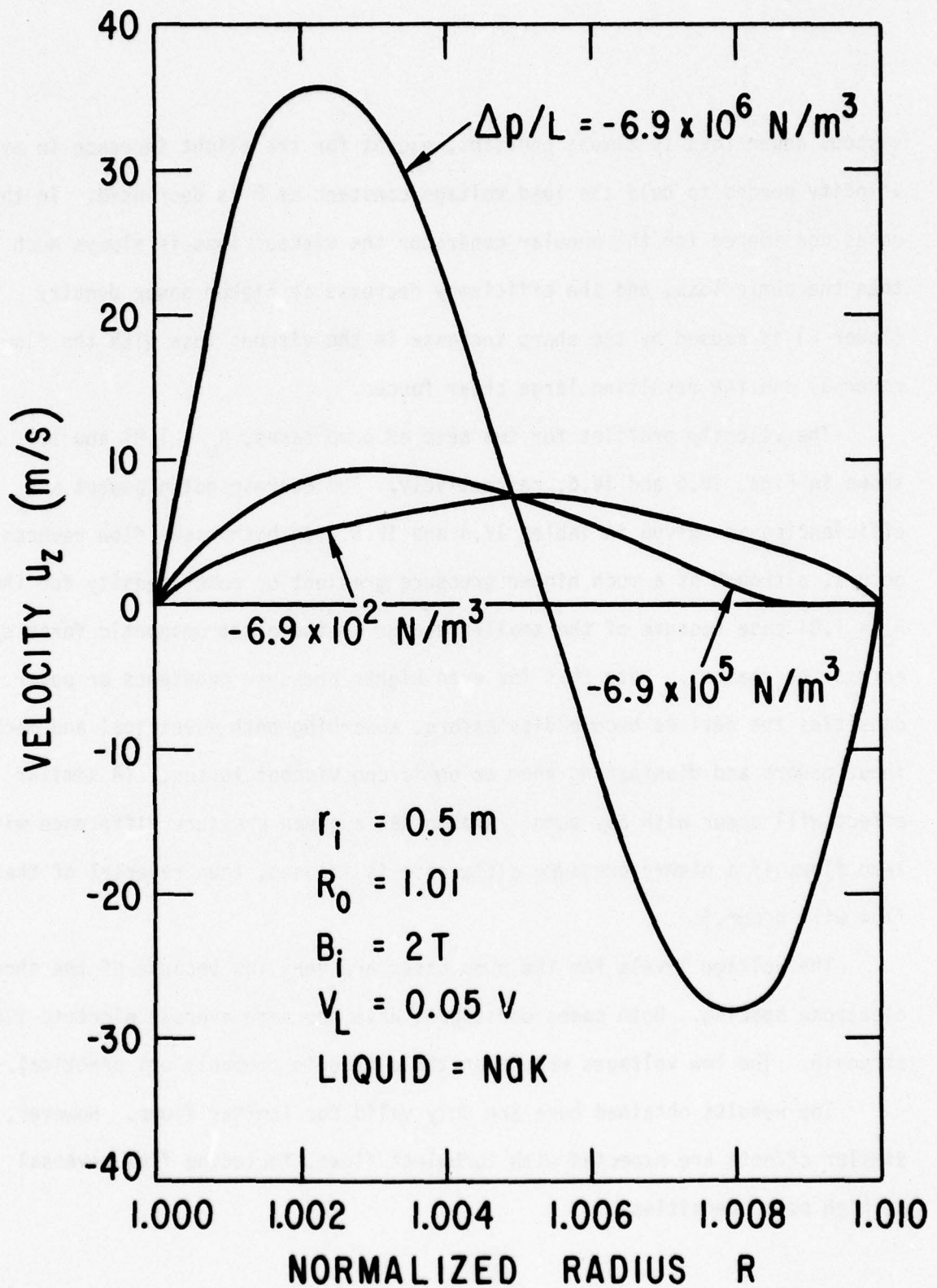


Figure IV.5. Velocity versus Radius as a Function of the Pressure Gradient for a Pump, $R_0 = 1.01$

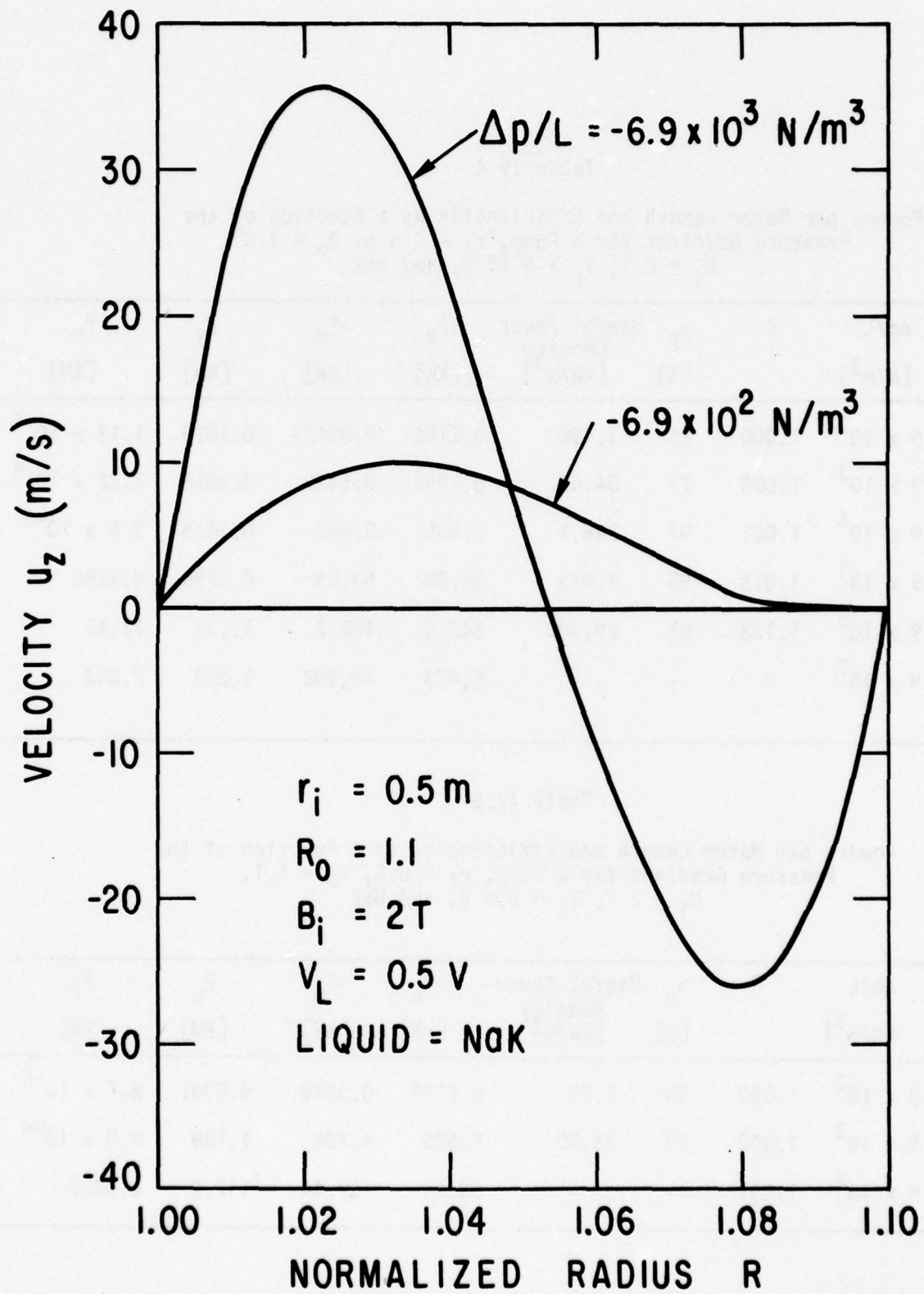


Figure IV.6 Velocity versus Radius as a Function of the Pressure Gradient for a Pump, $R_0 = 1.1$

Table IV.4

Powers per Meter Length and Efficiencies as a Function of the Pressure Gradient for a Pump, $r_i = 0.5$ m, $R_o = 1.01$,
 $B_i = 2$ T, $V_L = 0.05$ V, and NaK

$\Delta p/L$ [N/m ³]	F	η_p [%]	Useful Power Density [kW/m ³]	$-P_e$ [kW]	$-P_m$ [kW]	P_y [kW]	P_r [kW]
-6.9×10^2	1.000	25	3.466	0.2166	0.05473	0.1619	1.13×10^{-5}
-6.9×10^3	1.000	77	34.66	0.7092	0.5472	0.1618	1.22×10^{-4}
-6.9×10^4	1.001	97	346.1	5.635	5.465	0.1626	7.6×10^{-3}
-6.9×10^5	1.013	98	3,413	54.89	53.89	0.2798	0.7286
-6.9×10^6	1.153	85	29,300	547.5	462.7	12.34	72.47
-6.9×10^7	-	-	-	5,473	-2,992	1,222	7,243

Table IV.5

Powers per Meter Length and Efficiencies as a Function of the Pressure Gradient for a Pump, $r_i = 0.5$, $R_o = 1.1$,
 $B_i = 2$ T, $V_L = 0.5$ V, and NaK

$\Delta p/L$ [N/m ³]	F	η_p [%]	Useful Power Density [kW/m ³]	$-P_e$ [kW]	$-P_m$ [kW]	P_y [kW]	P_r [kW]
-6.9×10^2	1.000	95	3.73	0.6151	0.5849	0.0301	8.7×10^{-6}
-6.9×10^3	1.000	80	36.30	5.985	4.796	1.189	8.3×10^{-4}
-6.9×10^4	1.001	-	-	59.68	-57.44	117.0	0.0825

IV.5 Armature Reaction with Constant Velocity

The effect of the axial variation of the magnetic flux density and the (electric) current density caused by the current in the fluid is considered here. The three different connections to complete the load circuit, shown in Fig. IV.7, are:

1. At the downstream end,
2. At the upstream end, and
3. At both ends.

The three connections, their different effects on the magnetic field, and the resulting performances are discussed in the following material.

IV.5.1 Downstream Connection

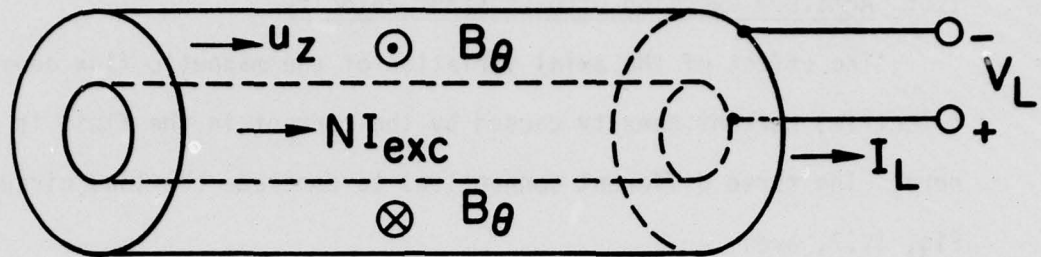
If the load is connected to the downstream ends of the electrodes, then the z-directed load current flowing along the inner electrode is in the same direction as the exciting current for a generator, Fig. IV.7. Thus, the induced magnetic field due to the load current reinforces the applied field, and the total field is every place greater than the applied field (except at the generator entrance where the induced field is zero).

The applied field is given by Eq. IV.15, and the total field is

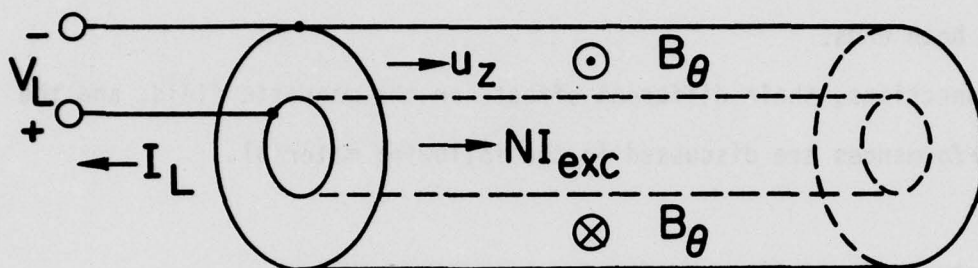
$$B_{\theta}(r,z) = \frac{\mu_0 NI_{exc}}{2\pi r} + \mu_0 \int_0^z J_r(r,z') dz' \quad (IV.43)$$

from Eq. IV.14 and conservation of charge. The electric field E_r must vary as $1/r$ from conservation of charge or Eq. IV.8, and Eq. IV.9; and in terms of V_L ,

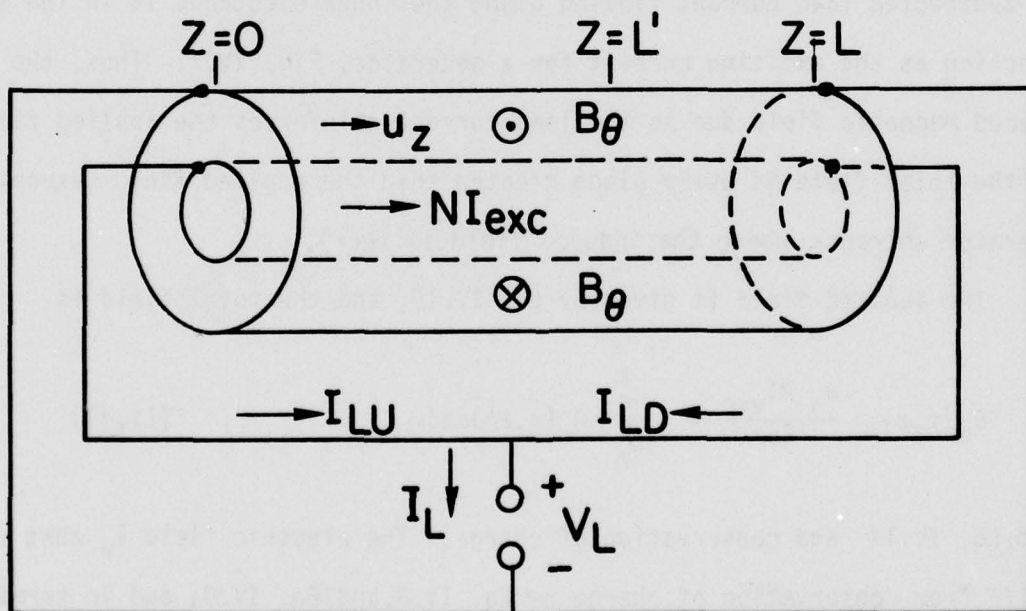
$$E_r = - \frac{V_L}{r \ln R_0} \quad (IV.44)$$



(a) DOWNSTREAM CONNECTION



(b) UPSTREAM CONNECTION



(c) BOTH ENDS CONNECTION

Figure IV.7 Load Connections for Armature Reaction Calculations

from Eq. IV.17. Substituting into Ohms law, Eq. IV.9, gives

$$J_r(r,z) = \frac{-\sigma V_L}{r \ln R_0} + \frac{R_m}{L} \left[\frac{NI_{exc}}{2\pi r} + \int_0^z J_r(r,z') dz' \right], \quad (IV.45)$$

where

$$R_m = \mu_0 \sigma u_z L \quad (IV.46)$$

is the magnetic Reynolds number. Solving Eq. IV.45 yields

$$J_r(r,z) = \left[\frac{R_m NI_{exc}}{2\pi r L} - \frac{\sigma V_L}{r \ln R_0} \right] e^{R_m z/L}; \quad (IV.47)$$

and, from Eqs. IV.43 and IV.16,

$$B_\theta(r,z) = \frac{\mu_0 NI_{exc}}{2\pi r} e^{R_m z/L} + \frac{V_L}{u_z r \ln R_0} [1 - e^{R_m z/L}] \quad (IV.48)$$

and

$$I_L = \left[NI_{exc} - \frac{2\pi V_L}{\mu_0 u_z \ln R_0} \right] (e^{R_m} - 1). \quad (IV.49)$$

From comparing Eq. IV.49 with the equivalent circuit, Fig. IV.2, V_{oc} is given by Eq. IV.27 for the ideal case, constant velocity with no armature reaction, since there is no armature reaction for open circuit. The internal resistance for this case,

$$R_i = \frac{R_m \ln R_0}{2\pi L \sigma (e^{R_m} - 1)}, \quad (IV.50)$$

is always less than the value for the ideal case, Eq. IV.28. The reduced value for R_i occurs because the total magnetic flux in the generator increases with

loading, and this acts to compensate for the increased ohmic voltage drop.

The Lorentz force integrated over the total channel volume is

$$F_{em} = \frac{-\mu_o \ln R_o (NI_{exc})^2 (1 - F)}{4\pi} [2F(e^{R_m} - 1) + (1 - F)(e^{2R_m} - 1)], \quad (IV.51)$$

From this plus the viscous pressure drop, Eq. IV.21, the mechanical input power can be calculated. The ohmic power loss in the fluid is

$$P_r = \frac{\sigma L \pi}{R_m \ln R_o} (V_{oc} - V_L)^2 (e^{2R_m} - 1). \quad (IV.52)$$

The remaining powers and efficiencies can be calculated from the equations in Section IV.2.

IV.5.2 Upstream Connection

If the load is connected to the upstream ends of the electrodes, then the z-directed load current flowing along the inner electrode is in the opposite direction to the exciting current, Fig. IV.7. For this case the induced magnetic field opposes the applied field, the total field is everywhere less than the applied field (except at the generator exit where the induced field is zero), and the reduction in the total magnetic flux in the generator is reflected in a larger internal resistance.

The procedure used to determine the equations for the upstream connection is the same as for the downstream connection. The results are:

$$B_{\theta}(r, z) = \frac{\mu_0 NI_{exc}}{2\pi r} - \mu_0 \int_L^z J_r(r, z') dz', \quad (IV.43a)$$

$$J_r(r, z) = \left[\frac{R_m NI_{exc}}{2\pi r L} - \frac{\sigma V_L}{r \ln R_0} \right] e^{R_m(z/L - 1)} \quad (IV.47a)$$

$$B_{\theta}(r, z) = \frac{\mu_0 NI_{exc}}{2\pi r} e^{R_m(z/L - 1)} + \frac{V_L}{u_z r \ln R_0} (1 - e^{R_m(z/L - 1)}),$$

$$I_L = \left[NI_{exc} - \frac{2\pi V_L}{\mu_0 u_z \ln R_0} \right] (1 - e^{-R_m}), \quad (IV.48a)$$

$$R_f = \frac{R_m \ln R_0}{2\pi L \sigma (1 - e^{-R_m})}, \quad (IV.49a)$$

and

$$F_{em} = \frac{-\mu_0}{4\pi} \ln R_0 (NI_{exc})^2 (1 - F) [(1 - F)(1 - e^{-2R_m}) + 2F(1 - e^{-R_m})]. \quad (IV.51a)$$

Note that V_{oc} is unchanged, and R_f is always greater than the value for the ideal case, Eq. IV.28.

IV.5.3 Both Ends Connection

With the load connected to both ends of the generator, Fig. IV.7, the generator is split into two regions by the location $z = L'$ where the component of the load current flowing along the axis is zero. The region for $z < L'$ behaves like a generator with the upstream connection, the region with $z > L'$ behaves like a generator with the downstream connection, and the total properties can be determined from the sum of the two regions using the equations from Sections IV.5.1 and IV.5.2. For example, the load current is given by

$$I_L = I_{LU} + I_{LD} = \left[NI_{\text{exc}} - \frac{2\pi V_L}{\mu_o u_z \ln R_o} \right] \left(e^{R_m \frac{(L-L')}{L}} - e^{-R_m L'/L} \right), \quad (\text{IV.49b})$$

where R_m is based on the total length L .

The location of L' would normally be determined by the voltage drop along the inner electrode. Since the electrode is assumed to be an equipotential here, it is not possible to calculate a value for L' .

IV.5.4 Numerical Example

The powers and efficiencies for one set of parameters are shown in Table IV.6 for the three connections, and the magnetic flux densities and current densities are shown in Figs. IV.8 and IV.9. For comparison, the values with the armature reaction ignored are also shown. The value of $R_m = 4.939$ is not large, yet the effects are dramatic. In fact, the downstream connection results are not realistic, the pressure gradient and magnetic flux density both become unrealistically large. (No iron is used, so that magnetic saturation is not a factor.) The upstream connection is realizable, but the power density is low. The choices $u_z = 15$ m/s and $\sigma = 2.62 \times 10^5$ mhos/m (0.1 times σ of NaK, characteristic of a high-void-fraction flow) were made to restrict R_m to small values. The excitation was chosen to yield $B_i = 3$ T with no armature reaction.

Similar effects due to armature reaction occur for rectangular geometries. However, it is easy to compensate rectangular generators by returning the load current through the magnet air gap. For an annular geometry, compensation would mean running the load current through the fluid gap between the electrodes, and this would eliminate one prime advantage of the annular geometry--the lack of insulating walls between the two electrodes.

Table IV.6

Powers and Efficiencies With and Without Armature Reaction,
 $r_i = 1.0$ m, $R_0 = 1.1$, $L = 1$ m, $u_z = 15$ m/s, $V_L = 3.903$,
 $F = 0.91$, $\sigma = 2.62 \times 10^5$ mhos/m, and $R_m = 4.939$

	Armature Reaction Ignored	Connection		
		Downstream	Upstream	Both Ends, $L' = 0.8$ m
I_L [MA]	4.445	124.7	0.8936	2.399
P_e [MW]	17.92	502.8	3.602	9.673
P_m [MW]	19.17	2,759	3.824	10.61
P_r [MW]	1.14	2,256	0.1158	0.835
P_d^* [MW/m ³]	27.16	762.1	5.46	14.66
$\Delta p/L$ [N/m ³]	1.937×10^6	2.789×10^8	3.865×10^5	1.073×10^6
η_g [%]	93.5	18.2	94.2	91.1
B_i (z=0) [T]	3.0	3.0	2.821	2.823
B_i (z=L) [T]	3.0	27.94	3.00	3.303

* P_d = useful power density

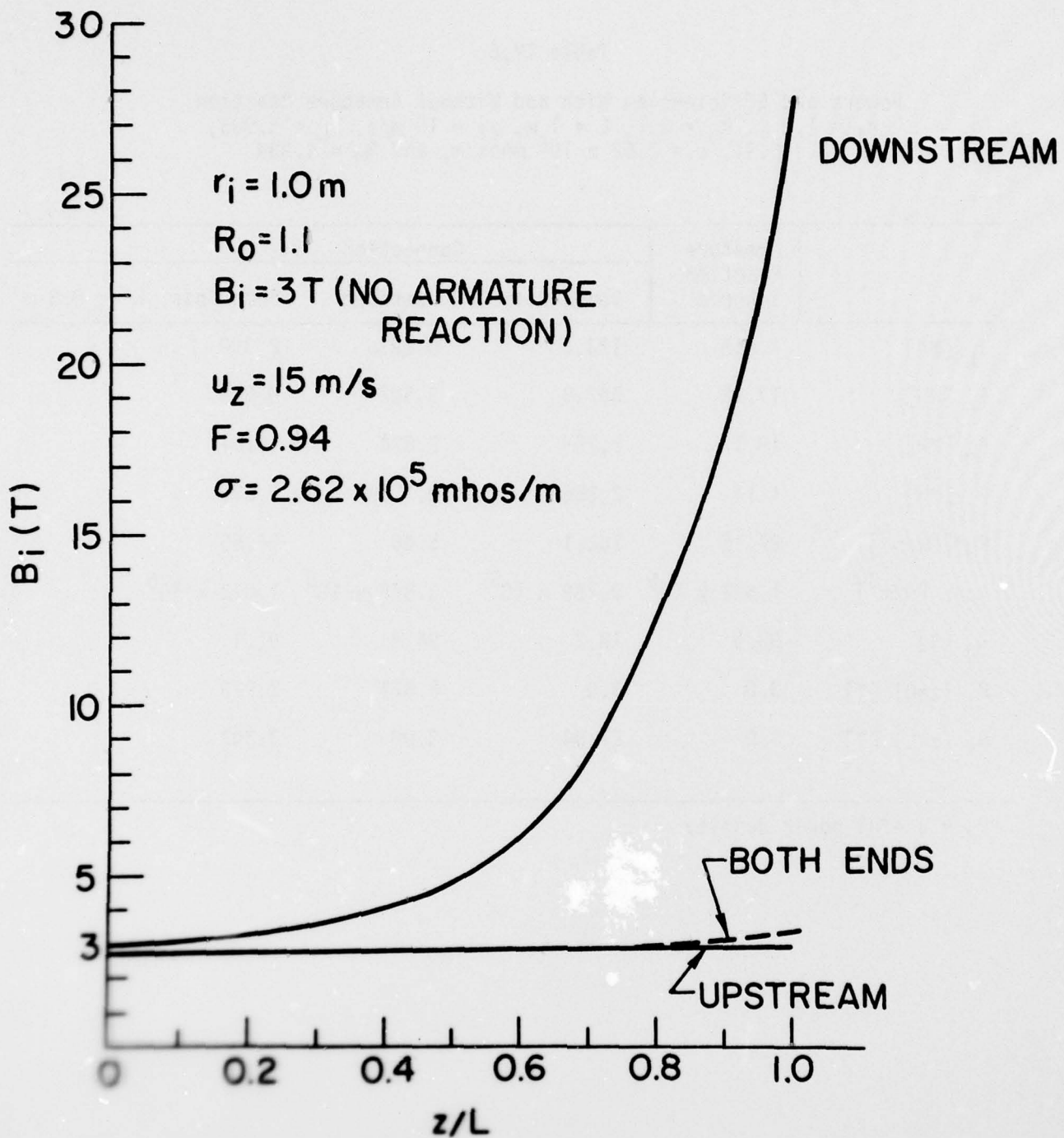


Figure 10.2 Magnetic Flux Density at Inner Radius with Armature Reaction versus Axial Location

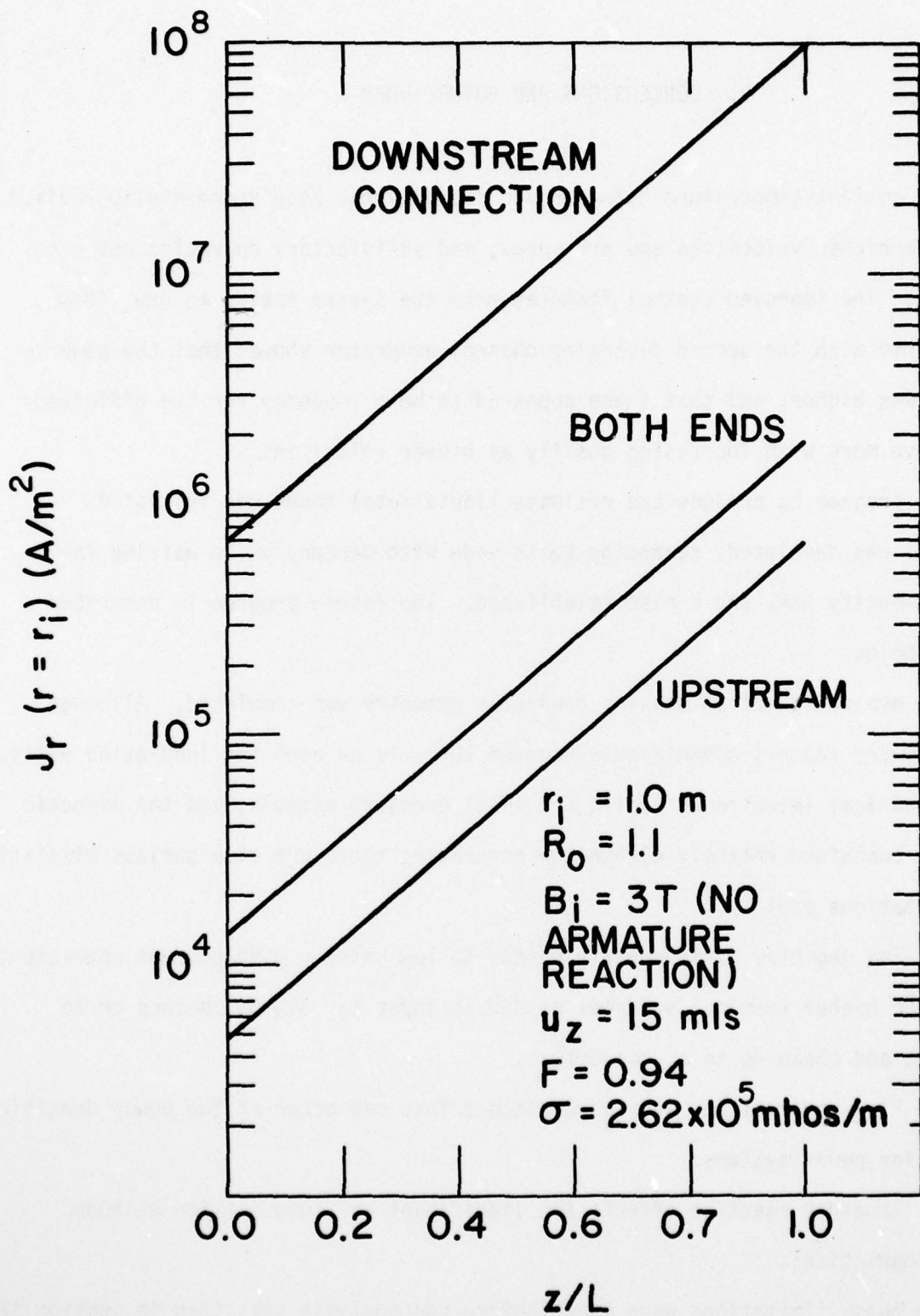


Figure IV.9 Current Density at Inner Radius with Armature Reaction Versus Axial Location

V. CONCLUSIONS AND FUTURE WORK

The ambient-temperature NaK-nitrogen facility has been successfully revised to handle higher velocities and pressures, and satisfactory operation has been obtained. The improved control features make the system easier to use. New experiments with the second diverging-channel generator showed that the power density was higher, and that there appeared to be a tendency for the efficiency to improve more with increasing quality at higher velocities.

The program to produce and evaluate liquid-metal foams was initiated. Equipment was developed, screening tests made with mercury while waiting for the high-purity NaK, and a plan established. The future program is described briefly below.

The evaluation of an annular generator geometry was completed. Although this geometry appears advantageous because there is no need for insulating walls, the cylindrical (electrode) shells are ideal pressure vessels, and the magnetic field is contained entirely within the generator; there are also serious limitations. The limitations are:

1. The geometry is inherently suited to low voltage high-current operation, not to the higher terminal voltages needed as input to acyclic motors or to efficient and cheap dc to ac converters.
2. Flow reversal and increased viscous loss can occur at the power densities desired for power systems.
3. Armature reaction effects are significant and compensation methods appear impractical.

Although these limitations were known before the analysis described in Section IV was performed, the analysis was necessary to quantify the effects. Based on this

analysis, this annular geometry does not appear attractive for either generator or pump operation.

The desired next steps in the liquid-metal MHD program are described below.

V.1 Higher Velocities and Pressures

The motivations for tests at higher liquid velocities are to reduce the slip loss due to the relative phase velocities, as experimental research has demonstrated that this loss can be decreased by increasing the liquid velocity,³ and to test the generator at velocities typical of practical generators. In the experiments to date except for a few recent runs, the liquid velocity has been limited to about 12 m/s. The revised facility allows generator operation at higher liquid velocities or flow rates and higher pressures. Testing of the existing diverging channel will continue at liquid flow rates up to about 10.9 kg/s (200 gpm), versus the previous limit of about 6 kg/s (110 gpm). This generator was designed for lower velocities and has an operating pressure range up to about 0.72 MPa absolute (90 psig), so that operation at higher velocities will require a reduced magnetic field strength.

A new generator will be designed and built to utilize the full loop capability of 10.9 kg/s and 1.48 MPa absolute (200 psig). This will allow high velocities with high field strengths, and variation of the generator pressure range with a maximum generator exit pressure of 1.14 MPa absolute (150 psig). This generator will have a different taper to fit the different design pressure ratio. Also, the maximum void fraction in the generator should be increased--this will be aided by a reduced velocity slip ratio.

V.2 Foams

The initial steps of the program to evaluate foams in MHD generators were described in Section II.3. In the next year attention will be focussed on identifying surface-active agents suitable for NaK, and plans should be developed for testing NaK foams in a generator. Bubbling tests with NaK and various additives will be part of the screening program, along with measurements of surface tension, viscosity, and wetting properties. NaK was chosen for the initial tests because of extensive experience with NaK in generators, and thus the ability to see the change in generator performance due to the use of a foam in minimum time and for minimal cost. If the NaK test results are positive, then effort will be directed toward finding foams suitable for use in practical MHD systems. Methods of separating the gas and liquid phases after the MHD generator for a foam must also be considered.

V.3 Improved Local Diagnostics

Improved local diagnostics are needed to obtain a better understanding of two-phase flows in a magnetic field. The data to be measured include direct local values of liquid and gas velocities, void fractions, bubble diameters, pressures, and temperatures. Measurement techniques to be evaluated include: (1) conductivity probes, both single and multiple, for void fractions, bubble sizes, and bubble velocities; (2) hot-film probes for liquid and gas velocities, void fractions, and bubble sizes; and (3) microthermocouples for gas and liquid temperatures. These techniques have been used successfully for air-water two-phase flows, but have not been tried with liquid metals or magnetic fields. Special electronics and data-processing techniques may be required.

This local data is needed to develop and evaluate improved analytical models for two-phase flows, Section V.4. Thus, a program to develop the measurement techniques should be initiated. First tests should use the air-water facility described in Reference 4 before incorporation into the ambient-temperature NaK-nitrogen loop.

V.4 Analytical Models for the Two-Phase Flow in the Generator

Further analytical studies on the two-phase flow in the MHD generator should be carried out in parallel with the above efforts. The experimental data, especially that from the improved local diagnostics as it becomes available, will be used in developing and evaluating these models. The primary goals are a better understanding of and model for the two-phase flow at high void fractions in a practical generator. The conditions for transitions between bubbly, churn-turbulent, slug, and annular flows at high void fractions may be explored. Of particular importance are the effects on generator performance of velocity, void fraction, and conductivity distributions across the channel, i.e., parallel to either the applied magnetic field or the current. These have not been included in any model to date except for a simple boundary-layer analysis.³

V.5 Imperfect Compensation

Most analyses of two-phase MHD generators have assumed perfect compensation, i.e., the generator current is returned through the air gap in the magnetic circuit in such a fashion that the applied magnetic field is not changed by the generator current. This may not be true in practice because of end currents, non-uniform current distributions in the generator and/or compensating conductors,

and compensating conductors that are longer than the electrodes as in the present generator. The development of an analytical model for the generator with imperfect compensation has been initiated. Future plans include experimental verification of the model.

REFERENCES

1. L. C. Pittenger, et al., "Experimental Two-Phase Liquid-Metal MHD Generator Program," Report No. ANL/ETD-72-07, Argonne National Laboratory, Argonne, IL, June 1972.
2. W. E. Amend, et al., "Experimental Two-Phase Liquid-Metal Magneto-hydrodynamic Generator Program," ANL/ENG-73-02, Argonne National Laboratory, Argonne, IL, June 1973.
3. M. Petrick, et al., "Experimental Two-Phase Liquid-Metal Magneto-hydrodynamic Generator Program," ANL/ENG-75-02, Argonne National Laboratory, Argonne, IL, January 1975.
4. M. Petrick, et al., "Experimental Two-Phase Liquid-Metal Magneto-hydrodynamic Generator Program," ANL/ENG-76-04, Argonne National Laboratory, Argonne, IL, November 1976.
5. M. Petrick, W. E. Amend, E. S. Pierson, and C. Hsu, "Investigation of Liquid-Metal MHD Power Systems," Report No. ANL/ETD-70-12, Argonne National Laboratory, Argonne, IL, December 1970.

APPENDIX A
SUMMARY OF EXPERIMENTAL GENERATOR DATA
AUGUST 1975 TO SEPTEMBER 1976

Date	Run Number	Mass Flow Rate		Magnetic Flux Density B [T]	Load Resistance R_L [$m\Omega$]	Load Voltage V_L [V]	Pressure		Power Output P_e [kW]	Average Void Fraction α
		NaK \dot{m}_e [kg/s]	N_2 \dot{m}_g [kg/s]				Inlet P_{in} [psia]	Exit P_{out} [psia]		
8-12-76	1	6.025	0	1.245	∞	.509	63.3	37.5	0	0
	2	6.115	.0125	1.246	∞	.717	57.7	34.2	0	.277
	3	6.025	.03175	1.244	∞	.932	57.1	35.2	0	.480
	4	6.025	.0507	1.245	∞	1.102	59.5	36.8	0	.558
	5	6.070	.0655	1.245	∞	1.257	60.7	36.0	0	.652
8-16-76	1	12.140	0	1.245	∞	.996	88.7	31.0	0	0
	2	12.095	.0135	1.235	∞	1.316	74.3	26.4	0	.184
	3	11.560	.0359	1.234	∞	1.784	78.4	31.0	0	.450
8-18-76	1	6.160	.0351	1.235	.2706	.867	88.4	34.0	2.78	.495
	2	6.003	.0516	1.238	.271	.932	92.6	36.3	3.21	.587
	3	6.025	.0672	1.235	.271	1.010	93.5	33.7	3.76	.678
	4	6.025	.0130	1.240	.2708	.665	80.3	31.5	1.63	.273
	5	6.025	0	1.253	.264	.470	81.1	35.0	.837	0
	6	6.025	.0654	1.235	.270	.931	77.0	18.5	3.21	.672
9-19-76	1	6.038	0	1.248	.2644	.476	65.0	18.3	.856	0
	2	6.025	.01396	1.233	.2709	.852	70.7	15.5	2.70	.524
	3	6.025	.0356	1.230	.2704	.725	65.4	16.4	1.94	.388
	4	6.025	0	1.25	∞	.492	45.1	18.1	0	0
	5	11.825	0	1.265	∞	.982	64.3	15.5	0	0
	6	6.070	.01231	1.236	∞	.827	39.2	17.5	0	.435
	7	6.025	.03078	1.235	∞	1.102	36.8	21.7	0	.608

Date	Run Number	Mass Flow Rate		Magnetic Flux Density B [T]	Load Resistance R _L [mΩ]	Load Voltage V _L [V]	Pressure		Power Output P _e [kW]	Average Void Fraction σ
		NaK m _g [kg/s]	N ₂ m _g [kg/s]				Inlet P _{in} [psia]	Exit P _{out} [psia]		
8-24-76	1	6.02	0	1.223	.240	.466	81.6	35.4	.903	0
	2	5.98	.06838	1.222	.2468	.937	93.0	26.6	3.56	.621
	3	6.07	.05049	1.227	.2475	.885	91.5	35.3	3.13	.547
	4	6.025	.03512	1.227	.2471	.824	87.4	33.7	2.75	.477
8-25-76	1	6.025	.07792	1.225	.2461	1.003	95.3	37.6	4.08	.542
	2	12.05	.06697	1.26	∞	1.988	83.2	34.0	0	.394
	3	6.025	.01372	1.225	.2441	.662	87.5	36.0	1.80	.161
	4	6.07	0	0	∞	0	31.8	31.7	0	0
9-2-76	1	12.09	0	0	∞	0	32.0	37.5	0	0
	2	6.025	.03564	.805	∞	.713	42.7	35.1	0	.574
	3	5.98	.05139	.807	∞	.822	45.0	35.3	0	.637
	4	6.07	.01393	.806	∞	.544	43.7	34.3	0	.390
	5	6.025	0	.808	∞	.313	44.3	32.2	0	0
	6	12.09	.05136	.805	∞	1.439	56.3	30.8	0	.438
9-9-76	1	12.09	0	0	∞	0	33.3	38.0	0	0
	2	5.98	.05797	.801	∞	.866	40.5	36.4	0	.734
9-13-76	1	18.03	0	0	∞	0	44.8	47.7	0	0
	2	5.98	.09896	1.35	.261	1.008	97.7	34.8	3.89	.581
9-15-76	1	12.14	0	.805	.251	.617	78.0	36.3	1.52	0
	2	11.91	.09533	.6	.260	1.160	74.5	28.4	5.18	.601
	3	11.96	.07093	.595	.259	1.018	71.7	33.2	4.00	.511
	4	12.095	.03775	.603	.259	.825	65.5	30.3	2.63	.389
	5	12.21	0	.620	.251	.472	54.2	28.7	.887	0
	6	6.025	.04863	.605	.259	.511	51.0	34.3	1.01	.546

Date	Run Number	Mass Flow Rate		Magnetic Flux Density B [T]	Load Resistance R_L [m Ω]	Load Voltage V_L [V]	Pressure		Power Output P_e [kW]	Average Void Fraction α
		NaK \dot{m}_e [kg/s]	N ₂ \dot{m}_g [kg/s]				Inlet P_{in} [psia]	Exit P_{out} [psia]		
9-17-76	1	6.151	0	.6	.250	.232	47.0	36.1	.215	0
	2	6.002	.01261	.6	.255	.344	49.5	36.4	.464	.317
	3	5.98	.03318	.595	.258	.451	52.0	36.8	.788	.520
	4	6.07	.06330	.595	.259	.539	53.8	35.1	1.12	.610
	5	11.915	.07023	.588	.373	1.068	64.2	32.0	3.06	.541
9-20-76	1	5.980	0	.599	∞	.238	43.9	36.6	0.	0
	2	6.025	.0135	.613	∞	.403	41.8	35.4	0	.359
	3	6.025	.0348	.598	∞	.543	41.7	35.8	0	.585
	4	6.025	.0502	.598	∞	.638	42.9	34.4	0	.637
	5	5.98	.06378	.602	∞	.695	43.7	35.5	0	.726

REPORT DOCUMENTATION PAGE		READ INSTRUCTIONS BEFORE COMPLETING FORM
1. REPORT NUMBER ANL/MHD-77-3	2. GOVT ACCESSION NO.	3. RECIPIENT'S CATALOG NUMBER
4. TITLE (and Subtitle) EXPERIMENTAL TWO-PHASE LIQUID-METAL MAGNETOHYDRODYNAMIC GENERATOR PROGRAM		5. TYPE OF REPORT & PERIOD COVERED Annual Report, August 1975 to September 1976
		6. PERFORMING ORG. REPORT NUMBER ANL/MHD-77-3 ✓
7. AUTHOR(s) M. Petrick, G. Fabris, E. S. Pierson, D. Carl, A. K. Fischer, C. E. Johnson		8. CONTRACT OR GRANT NUMBER(s) N00014-76-F-0026 <i>New</i>
9. PERFORMING ORGANIZATION NAME AND ADDRESS Argonne National Laboratory 9700 South Cass Avenue Argonne, Illinois 60439		10. PROGRAM ELEMENT, PROJECT, TASK AREA & WORK UNIT NUMBERS Task No. NR099-404
11. CONTROLLING OFFICE NAME AND ADDRESS Office of Naval Research (Code 473) Department of the Navy Arlington, Virginia 22217		12. REPORT DATE September 1977
		13. NUMBER OF PAGES 92
14. MONITORING AGENCY NAME & ADDRESS (if different from Controlling Office) Same as 11		15. SECURITY CLASS. (of this report) Unclassified
		15a. DECLASSIFICATION/DOWNGRADING SCHEDULE
16. DISTRIBUTION STATEMENT (of this Report) Approved for public release; distribution unlimited		
17. DISTRIBUTION STATEMENT (of the abstract entered in Block 20, if different from Report)		
18. SUPPLEMENTARY NOTES		
19. KEY WORDS (Continue on reverse side if necessary and identify by block number)		
armature reaction	load voltage	quality
bubble parameter	magnetohydrodynamics	slip
generator efficiency	pressure gradient	two-phase
liquid metals		void fraction
20. ABSTRACT (Continue on reverse side if necessary and identify by block number)		
<p>The revised ambient-temperature NaK-nitrogen facility is described. The maximum liquid flow rate and generator inlet pressure are 10.9 kg/s (200 gpm) and 1.48 MPa absolute (200 psig), respectively, compared with the previous values of 6 kg/s (110 gpm) and 0.72 MPa absolute (90 psig). Satisfactory loop operation has been obtained, and new experiments with the second diverging-channel generator were completed. The principal experimental results were a higher power density for the same generator operating conditions, and an <i>→ save</i></p>		

20. Abstract (contd.)

apparent tendency for the efficiency to improve more with increasing quality at higher velocities than lower velocities.

An evaluation of an annular generator geometry is presented. The advantages and disadvantages of the geometry are described, the equations developed, and solutions obtained for three cases--constant velocity and no armature reaction, laminar flow with no armature reaction, and armature reaction with constant velocity. Numerical examples show that: (1) the attainable terminal voltages appear to be very low, (2) flow reversal and large viscous loss occur at or below the desired power densities, and (3) armature reaction effects are important and compensation techniques appear impractical. Thus, this annular geometry does not appear attractive for either generator or pump operation.

The initial steps in the program to produce and evaluate liquid-metal foams are described. The future directions of the experimental generator program, including foams, are discussed.

Distribution List For

Annual Report On

Liquid-Metal Magneto hydrodynamic Power

<u>Activity</u>	<u>No. of Copies</u>
Administrative Contracting Officer DCASO, Huntsville 2109 West Clinton Avenue Huntsville, Alabama 35805 Attn: Mr. D. W. VanBrunt	1
Office of Naval Research Department of the Navy Arlington, Virginia 22217 Attn: Mr. J. A. Satkowski, Code 473 Attn: Mr. B. Friedman, Code 221C	3 2
Commanding Officer Office of Naval Research Branch Office 536 South Clark Street Chicago, Illinois 60605	1
Director U.S. Naval Research Laboratory Washington, D.C. 20390 Attn: Code 2629 Attn: Code 2627	6 6
Defense Documentation Center Cameron Station Alexandria, Virginia 22314	12
Commander Naval Sea Systems Command Department of the Navy Washington, D.C. 20360 Attn: Dr. John Huth, Chief Scientist Attn: Mr. R. M. Forsell, Code 08	1 1
Commanding Officer Air Force Office of Scientific Research Bolling Air Force Base Building 410 Washington, D.C. 20332 Attn: Dr. B. Wolfson	1
Commander Naval Underwater Systems Center Fort Trumbull New London, Connecticut 06320 Attn: Technical Library	1

AD-A046 951

ARGONNE NATIONAL LAB ILL ENGINEERING DIV

F/G 10/2

EXPERIMENTAL TWO-PHASE LIQUID-METAL MAGNETOHYDRODYNAMIC GENERAT--ETC(U)

SEP 77 M PETRICK, G FABRIS, E S PIERSON

N00014-76-F-0026

UNCLASSIFIED

ANL/MHD-77-3

NL

2 of 2

ADA046951



END

DATE

FILMED

1 -78

DDC

<u>Activity</u>	<u>No. of Copies</u>
General Electric Company Valley Forge Space Technology Center P.O. Box 8555 Philadelphia, Pennsylvania 19101 Attn: Dr. B. Zauderer	1
University of Maryland Department of Mechanical Engineering College Park, Maryland 20742 Attn: Dr. M. E. Talaat	1
Stanford University Department of Mechanical Engineering Stanford, California 94305 Attn: Professor R. H. Eustis	1
Rand Corporation 1700 South Main Street Santa Monica, California 90401 Attn: Technical Library	1
Jet Propulsion Laboratory 4800 Oak Grove Drive Pasadena, California 91103 Attn: Dr. D. G. Elliott	1
Energy Research and Development Administration Oak Ridge Operations Officer Reactor Division Oak Ridge, Tennessee 37830 Attn: Mr. J. Pidkowicz	1
University of Texas Department of Electrical Engineering Plasma Dynamics Research Laboratory Austin, Texas 78712 Attn: Dr. O. M. Friedrich, Jr.	1
Institute for Defense Analyses 400 Army-Navy Drive Arlington, Virginia 22202 Attn: Mr. R. Hamilton	1
Massachusetts Institute of Technology Department of Aeronautics and Astronautics Cambridge, Massachusetts 02139 Attn: Dr. J. Louis	1

<u>Activity</u>	<u>No. of Copies</u>
Los Alamos Scientific Laboratory P.O. Box 1664 Los Alamos, New Mexico 87544 Attn: Technical Library	1
Naval Surface Weapons Center Dahlgren, Virginia 22448 Attn: Technical Library	1
Superintendent U.S. Naval Postgraduate School Monterey, California 93940 Attn: Library, Code 0212	1
Commanding Officer Naval Ocean Research and Development Activity Bay St. Louis, Mississippi 39520 Attn: Technical Library	1
Officer in Charge Naval Ship Research and Development Laboratory Annapolis Division Annapolis, Maryland 21402 Attn: Special Projects Division Library, Code 421A	1 1
Commander Naval Weapons Center Propulsion Applied Research Group China Lake, California 93555 Attn: Technical Library	1
Air Force Aero Propulsion Laboratory AFAPL/POP-2 Wright Patterson Air Force Base, Ohio 45433 Attn: Mr. R. Cooper/55475	1
Commander Naval Surface Weapons Center White Oak Silver Spring, Maryland Attn: Technical Library	1
National Aeronautics and Space Administration Lewis Research Center 21000 Brookpark Road Cleveland, Ohio 44135 Attn: Dr. L. Nichols	1

<u>Activity</u>	<u>No. of Copies</u>
National Science Foundation Engineering Division Washington, D.C. 20550 Attn: Dr. Royal Rostenbach	1
Lawrence Livermore Laboratory Technical Information Department P.O. Box 808 Livermore, California 94550 Attn: Mr. H. Cheung Mr. O. Loper	1 1
Commandant U.S. Marine Corps, Code CSY-3 Headquarters, Marine Corps Washington, D.C. 20380	1
North American Rockwell Atomics International P. O. Box 309 Canoga Park, California 91304 Attn: Mr. J. C. Cochran	1
Knolls Atomic Power Laboratory Schenectady, New York 12301	1
University City Science Institute Power Information Center 3401 Market Street, Room 2210 Philadelphia, Pennsylvania 19104	1
Avco-Everett Research Laboratory 2385 Revere Beach Parkway Everett, Massachusetts 02149 Attn: Ray Janney	1
University of Tennessee Space Institute Tullahoma, Tennessee 37388 Attn: Dr. J. B. Dicks	1
Air Vehicle Corporation 8873 Balboa Avenue San Diego, California 92123 Attn: Dr. J. Rosciszewski	1
STD Research Corporation P.O. Box C, Arcadia Pasadena, California 91106 Attn: Dr. J. C. Cutting	1

<u>Activity</u>	<u>No. of Copies</u>
Cornell University Mechanical and Aerospace Engineering Ithaca, New York 14851 Attn: Professor E. Resler, Jr.	1
Case Institute of Technology Department of Electrical Engineering University Circle Cleveland, Ohio 44101 Attn: Dr. E. Reshotko	1
University of Pennsylvania Mechanical Engineering Department 335d and Locust Streets Philadelphia, Pennsylvania 19104 Attn: Dr. H. Yeh	1
California Institute of Technology 1201 East California Avenue Pasadena, California 91102 Attn: Technical Library	1
Colorado State University Department of Mechanical Engineering Fort Collins, Colorado 80521 Attn: Dr. H. E. Wilhelm	1
University of California Mechanical Engineering Department Davis, California 95616 Attn: Dr. M. Hoffman	1
Energy Research Corporation 15 Durant Avenue Bethel, Connecticut 06801 Attn: Technical Library	1
National Bureau of Standards U.S. Department of Commerce Boulder, Colorado 80302 Attn: Dr. Robert L. Powell	1
National Bureau of Standards U.S. Department of Commerce Washington, D.C. 20234 Attn: Dr. John Wachtman	1

<u>Activity</u>	<u>No. of Copies</u>
University of Florida College of Engineering 231 Aerospace Engineering Building Gainesville, Florida 32611 Attn: Dr. E. Rune Lindgren	1
Naval Material Command NAVMAT 0333 Washington, D.C. 20360 Attn: Mr. R. V. Vittucci	1
Defense Advanced Research Projects Agency 1400 Wilson Boulevard Arlington, Virginia 22209 Attn: Dr. George Donahue	1
Brown University Box D Providence, RI 02912 Attn: Dr. J. Kestin	1
The Rand Corporation 2100 M Street N.W. Washington, D. C. 20037 Attn: R. Y. Pei	1
U.S. Department of Energy MHD Program Office 20 Massachusetts Avenue Washington, D. C. 20545 Attn: M. Sluyter	1